High-resolution ambient noise imaging of geothermal reservoir using 3C dense seismic nodal array and ultra-short observation

Feng Cheng[1], Jianghai Xia[2], Jonathan Blair Ajo-Franklin[1], Michael Behm[3], Changjiang Zhou[2], Tianyu Dai[4], Chaoqiang Xi[2], Jingyin Pang[2], and Changwei Zhou[2]

[1]Rice University
[2]Zhejiang University
[3]Geo Data
[4]Nanchang University

November 22, 2022

Abstract

Tomographic imaging based on long-term ambient seismic noise measurements, mainly the phase information from surface waves, has been shown to be a powerful tool for geothermal reservoir imaging and monitoring. In this study, we utilize seismic noise data from a dense nodal array (192 3C nodes within 20km2) over a ultra-short observation period (4.7 days) to reconstruct surface waves and determine the high-resolution (0.2km) three-dimensional (3-D) S wave velocity structure beneath a rural town in Zhejiang, China. We report the advantage of cross-coherence over cross-correlation in suppressing pseudo-arrivals caused by persistent sources. We use ambient noise interferometry to retrieve high quality Rayleigh waves and Love waves. Body waves are also observed on the R-R component interferograms. We apply phase velocity dispersion measurements on both Rayleigh waves and Love waves and automatically pick more than 23,000 dispersion curves by using a Machine Learning technique. 3-D surface wave tomographic results after depth inversion indicate low-velocity anomalies (between -1% and -4%) from the surface to 2km depth in the central area. Combined with the conductive characteristics observed on resistivity profile, the low-velocity anomalies are inferred to be a fluid saturated zone of highly fractured rock. Joint interpretation based on HVSR measurements, and existing temperature and fluid resistivity records observed in a nearby well, suggests the existence of the high-temperature geothermal field through the fracture channel. Strong correlation between HVSR measurements and S wave velocity model sheds light on the potential of extraction of both amplitude and phase information from ambient noise.

High-resolution ambient noise imaging of geothermal reservoir using 3C dense seismic nodal array and ultra-short observation

Feng Cheng[1,2], Jianghai Xia[3], Jonathan B. Ajo-Franklin[1,2], Michael Behm[4], Changjiang Zhou[3], Tianyu Dai[5], Chaoqiang Xi[3], Jingyin Pang[3], Changwei Zhou[3,6]

[1]Dept. of Earth, Environmental, and Planetary Sciences, Rice University, 6100 Main St., Houston, TX 77005, USA
[2]Lawrence Berkeley National Laboratory, 1 Cyclotron Rd., Berkeley, CA 94720, USA
[3]School of Earth Sciences, Zhejiang University, 38 Zheda Rd., Hangzhou, Zhejiang 310027, China
[4]GEODATA Survey & Monitoring Group, Hans-Kudlich-Straße 28, A-8700 Leoben, Austria
[5]School of Information Engineering, Nanchang University, 999 Xuefu Rd., Honggutan New District, Jiangxi 330031, China
[6]Zhejiang Geophysical and Geochemical Prospecting Academy, Hangzhou, Zhejiang 310000, China

Key Points:

- Ambient noise data have been recorded using a dense nodal array (192 3C nodes within $20km^2$) over ultra-short observation period (4.7 days)
- Both surface waves (Rayleigh and Love waves) and P waves are identified in the cross-coherence functions
- S wave velocity model is consistent with existing geophysical data and suggests the existence of high-temperature geothermal resources at depth

Corresponding author: Jianghai Xia, `jhxia@zju.edu.cn`

Abstract

Tomographic imaging based on long-term ambient seismic noise measurements, mainly the phase information from surface waves, has been shown to be a powerful tool for geothermal reservoir imaging and monitoring. In this study, we utilize seismic noise data from a dense nodal array (192 3C nodes within $20km^2$) over a ultra-short observation period (4.7 days) to reconstruct surface waves and determine the high-resolution (0.2km) three-dimensional (3-D) S wave velocity structure beneath a rural town in Zhejiang, China. We report the advantage of cross-coherence over cross-correlation in suppressing pseudo-arrivals caused by persistent sources. We use ambient noise interferometry to retrieve high quality Rayleigh waves and Love waves. Body waves are also observed on the R-R component interferograms. We apply phase velocity dispersion measurements on both Rayleigh waves and Love waves and automatically pick more than 23,000 dispersion curves by using a Machine Learning technique. 3-D surface wave tomographic results after depth inversion indicate low-velocity anomalies (between -1% and -4%) from the surface to 2 km depth in the central area. Combined with the conductive characteristics observed on resistivity profile, the low-velocity anomalies are inferred to be a fluid saturated zone of highly fractured rock. Joint interpretation based on HVSR measurements, and existing temperature and fluid resistivity records observed in a nearby well, suggests the existence of the high-temperature geothermal field through the fracture channel. Strong correlation between HVSR measurements and S wave velocity model sheds light on the potential of extraction of both amplitude and phase information from ambient noise.

1 Introduction

Geothermal energy is one of the most promising renewable energy sources, particularly within the context of China's energy structure optimization, environmental protection measures, energy conservation, and rising pressure on emission reduction. By the end of 2020, renewable energy facilities, including solar, wind, geothermal and other types of energy, in China will supply 27% of total power generation, according to the government's 2016-2020 plan for renewable energy. However, geothermal resources accounted for only 0.6% of the total energy consumption in 2019 (Liu et al., 2019). Therefore, significant work is required for the development of national geothermal resources. Geothermal energy production converts heat energy stored in the Earth into energy forms useful for humans; in most implementations, geothermal energy production is clean, sustainable, and can provide baseload capacity to regional power grids (Tomac & Sauter, 2018). Geothermal energy resources can be classified into two types: shallow geothermal and deep geothermal resources (Ganguly & Kumar, 2012). Shallow geothermal energy is often tapped in the form of hot water or steam (e.g. hydrothermal production), while deep geothermal energy often takes the form of "hot dry rock" resources that usually exists at depths greater than 3–5 km beneath the Earth's surface (Rubio-Maya et al., 2015; Xie et al., 2020). China has enormous geothermal resource potential, however, low-temperature geothermal resources are more common than high-temperature ones. The high-temperature geothermal resources are located in the marginal zone of the plate with an abnormal tectonic activity, e.g., Himalayan and Taiwan geothermal belts, (Zhang et al., 2019). The low- and medium-temperature geothermal resources are mostly located in uplifted mountain-type and sedimentary basin areas within the plates (Long et al., 2015). Geothermal resources distributed in mountain fault zones are generally quite small in scale (Wang et al., 2017). Therefore, evaluation and utilization of low/medium-temperature geothermal energy dependent on the high-resolution geothermal reservoir imaging techniques.

Geothermal systems often give distinctive and fairly easily measured discontinuities in physical properties (e.g., high heat flow, low electrical resistivity, attenuation of high frequency elastic waves), and geophysical methods play a key role in geothermal reservoir exploration (Combs, 1978). For examples, a gravity survey can be used to study the depth of fill in intermontaine valleys, and to locate intrusive masses of rock (e.g., Santos & Rivas, 2009; Atef et al., 2016); magnetic surveys can be used to identify the boundaries to the flows in volcanic areas (e.g., Hochstein & Soengkono, 1997; Zaher et al., 2018); a combination of resistivity studies and heat flow determinations is advisable to search for zones of fracture permeability in the reservoir (e.g., Wright et al., 1985; Thanassoulas, 1991; Munoz, 2014); a seismic reflection survey can be used where there is a bedded structure to the subsurface to allow the recognition of faults by the disruption of the continuity of the bedding (e.g., Lüschen et al., 2011); a microseismic survey is also a widely used tool for studying activity on fracture zones in a prospect area since high temperature hydrothemal areas are characterized by a relatively high level of microearthquake activity (e.g., Ward, 1972; Combs & Hadley, 1977; Obermann et al., 2015). However, no one exploration technique is likely to be universally effective in defining a geothermal reservoir. Some methods lack the maturity of development to be used effectively under difficult conditions, while others become less useful for deep exploration because of lack of sensitivity (Keller, 1981). Considering the limitations of various methods, it is probably necessary to employ a wide variety of techniques.

Over the last decade, ambient noise interferometry techniques have found a variety of applications for geothermal reservoir imaging (e.g., Tibuleac et al., 2009; Tibuleac & Eneva, 2011; Obermann et al., 2015; Lehujeur et al., 2016, 2018; Spica et al., 2018; Martins et al., 2019, 2020; Planès et al., 2020). Compared to relatively expensive active seismic imaging methods, ambient noise imaging is a passive and low-cost approach. Following the pioneering work of Campillo and Paul (2003), ambient noise interferometry can be used to estimate an approximate Green's function between two receivers by cross-correlating the ambient seismic wave field (Shapiro & Campillo, 2004; Snieder, 2004; Wapenaar, 2004a; Bensen et al., 2007; Snieder et al., 2009; Nakata et al., 2015). This approach has been applied to characterize multiple scales of earth structure: from the global scale or continental scale deep-structure imaging in seismology (e.g., Yang et al., 2007; Lin et al., 2008; Yao & van der Hilst, 2009; Lin et al., 2009; Strobbia & Cassiani, 2011) to local scale exploration (e.g., Bakulin & Calvert, 2006; Wapenaar et al., 2008; Draganov et al., 2009; Nakata et al., 2011; Ali et al., 2013; Behm et al., 2014; Cheng et al., 2015, 2016; Nakata et al., 2016; Cheng et al., 2018; Behm et al., 2019; Castellanos et al., 2020).

To date, ambient noise interferometry is almost exclusively performed with surface waves tomography based on multiple-station (tens or more) networks and long-term (months or years) continuous observations (Lin et al., 2008; Martins et al., 2019; Planès et al., 2020). Here we investigate the potential of high-resolution (i.e., 0.2km) ambient noise imaging of geothermal reservoir using a dense seismic nodal array (i.e., 192 nodes within $20km^2$) over an ultra-short observation period (i.e., 4.7 days). In the following study, we present the acquisition and the main characteristics of the ambient seismic noise records obtained from a dense network deployed in a rural town in Zhejiang, China. We extract high quality Rayleigh waves and Love waves based on ambient noise interferometry, and automatically pick more than 23k phase velocity dispersion curves to allow three-dimensional (3-D) S wave velocity model construction. The model is finally discussed in the light of HVSR measurements and existing borehole records and resistivity surveys.

2 Area and Data

The area of investigation (Fig.1) stands on the eastern margin of the Jinqu basin in southeastern China, where the deep NE-SW Jiangshan-Shaoxing fault crosses the basin. The Jiangshan-Shaoxing fault is a major structural feature which traverses Zhejiang Province and divides it into two distinct geological zones, the northwest Yangtze paraplatform, a relatively stable tectonic area dominantly composed of sedimentary rocks ranging from the Sinian (Pre-Cambrian) System to the Lower Triassic Series, and the southeast South China fold system, which is commonly overlain by Yanshanian (Mesozoic to Cenozoic) volcanic and acid igneous rocks (Zhejiang, 1989). The fault itself has been active since

Proterozoic times when it was initiated (Ren, 1987). The pattern of heat flow in southeastern China has been investigated by Hu and Wang (2000) and Yuan et al. (2006). A high heat flow of 75-80mW/m^2 has been found in the Jinqu basin. Our survey region is centered in a rural town (Fig.1a), Andi, where surface hot water has been founded by residents in recent years.

Based on the 1:50000 geological map released by Zhejiang Geophysical and Geochemical Prospecting Academy (ZGGPA) in 2006 (Fig.1b), the survey zone mainly consists of the younger upper Jurassic system (J_3x, J_3d, J_3g) at the northern, central and southwestern region, and the older PreSinian system ($AnZch^2$) at the south. The alluvial deposits from the Quaternary system (Q_4) split the area. The Plum Creek River (the north blue line on Fig.1a) starts from north and crosses through the town area before it reaches a water reservoir (outlined by the blue lines on Fig.1a) at the southwest. Coarse-grained adamellites ($\eta\gamma$) are widely distributed in the south mountain areas and adamellite dykes are in unconformable contact with the baned biotite plagiogneiss of the PreSinian system; granite (ν) dykes are intruded in the fracture system by the rifting unconformity.

A total of 192 nodal seismic stations (Fairfield ZLand 3C 5Hz), as indicated by the triangles on Figure.1a, were deployed over Andi town with an average aperture around 4.8km. The nodes recorded continuously from 12:30 pm, May 9th 2019 to 7:45 am, May 14th 2019 (about 4.7 days) with the sampling frequency of 500Hz. The nodes were buried at 30 cm and coupled to the ground with 15-cm metallic spikes. The interstation distances vary from the nearest 100m to the farthest 4.7km. In addition to the nodal seismic survey, one 2-km-long CSAMT (controlled-source audio-frequency magnetotellurics) profile was available (the red line in Fig.1) for reference, and one test well (the white cross in Fig.1) was drilled in 2016 by ZGGPA.

3 Methods

3.1 Noise characteristics

To understand the temporal and spectral characteristics of the observed ambient noise records, we employed spectral analysis on the raw waveforms. For each station, we first split the continuous noise records into 1-min-long time segments without overlaps. We computer the power spectral density (PSD, McNamara & Buland, 2004) of the raw waveforms, and stack all segments along the time direction to build a time-frequency spectra image. The PSD spectrograms within each one-hour epoch are averaged together as the spectrogram at the corresponding epoch. Note that we did not correct the absolute amplitude of the PSD with the instrument response. The obtained spectrograms present strong temporal and spatial amplitude variations. The PSD difference between daytime and nighttime is around 10dB in spatial average. Figure.2 displays three examples of the vertical component spectrograms at different locations (indicated by the magenta triangles on Fig.1a), north (a), central (b) and south (c). Compared with the central station in the rural town area, the north station (Fig.2a) shows stronger noise energy as well as higher dominant frequencies (around 20-30 Hz) because of the existence of several busy highways and express roads that connect the northern urban city, Jinhua, with the surrounding rural towns. As for the central station (Fig.2b), it shows dominant frequencies around 10Hz which is similar as that in urban area, and the distinct daily pattern which reflects much regular human activities in the peaceful rural town compared with that on the north station. Several long duration and very narrow-band signals, visible as horizontal lines or spikes (as indicated by the double arrow around 4.2 Hz), were also observed; these seismic waves are most probably excited by rotating machinery operating at fixed frequencies, like electrical motors and gearboxes of industrial machinery (Plesinger & Wielandt, 1974; Groos & Ritter, 2009; Cheng et al., 2019). As for the south station located in the mountain area (Fig.2c), the PSD energy is generally 10dB lower than that in the central town area, and the weak daily pattern indicates the observed noise energy from the distant human activities. Note that the strong energy around 35Hz in the daytime of May 13th (highlighted by the gray box on Fig.2c) is supposed to be the signature from weather associated with rain and potentially thunder (Dean, 2017), and it is also consistent with the relative weak energy between 1 and 20Hz observed at the same duration on the central station (Fig.2b) which indicates less human activities affected by the rain weather. The similar seismic signature from weather has been successfully reported by Zhu and Stensrud (2019) by using a fiber-optic distributed acoustic sensing array.

We also apply beamforming analysis (Lacoss et al., 1969; Rost & Thomas, 2002; Gerstoft & Tanimoto, 2007) on the raw waveforms, to figure out the spatial distribution of the seismic noise sources, which is necessary for our further ambient noise interferometry work. Beamforming analysis presents the constructive summation of all signals shifted appropriately in the time or frequency domain for the matching azimuth (clockwise from the north) and slowness. Figure.3 displays the averaged beam energy at different frequency bands based on vertical component (the upper panels) and the north horizontal component (the bottom panels). Beam energy plots below 1.0Hz (Fig.3a1 and Fig.3b1) show distinct source energy from the southeastern direction with apparent velocity >3km/s, and we infer the source to be primary and secondary microseism noise i.e. nonlinear interactions of ocean waves (Ardhuin et al., 2015) with the southeastern coast of Zhejiang province (as indicated by the China map on Fig.1). For the frequency band between 1Hz and 5Hz, we observe distinct spectral energy peak from the north (Fig.3a2 and Fig.3b2) with an apparent velocity of $\sim$2.5km/s; the noise source is likely surface waves generated by activity 18 km to the north in the urban city of Jinhua as well as the northern traffic lines. For the higher frequency band between 5 and 10Hz, we observe almost an isotropic noise distribution in the beam domain (Fig.3a3 and Fig.3b3), except for the southeastern direction where the mountain area located. In general, it indicates a relative homogeneous source distribution which is advantageous for ambient noise interferometry (Weaver & Lobkis, 2001; Wapenaar, 2004b). It is worth noting that the weak beam energy with apparent velocity >4km/s can be observed on the horizontal component with frequency >1Hz (Fig.3b2 and Fig.3b3), as well as the vertical component with frequency >5Hz (Fig.3a3). Beam energy with higher frequencies and higher velocities is likely associated with body waves which will be further discussed. Accounting for the body wave energy, we observed the horizontal component (Fig.3b3) presents the relative stronger energy than the vertical component (Fig.3a3).

3.2 Ambient Noise Interferometry

We follow the workflow of Bensen et al. (2007) to preprocess the recorded noise prior to retrieval of surface waves by ambient noise interferometry. We first downsample the raw data to 100Hz; next we split the continuous noise waveforms into a series of 1-min-long time segments without overlaps, and remove means and trends of the short noise segment followed by tapering; next we utilize temporal normalization to attenuate artifacts, e.g., near-field interferences and earthquakes, by using a running absolute mean filter (e.g. Bensen et al., 2007); finally, spectral normalization is utilized to extend the frequency band with a frequency-domain whitening approach, which computes the running smoothed amplitude of complex Fourier spectrum as the whiten weights with a moving window of 0.5% length of the frequency series.

Two main algorithms exist for empirical Green's function (EGF) extraction from ambient noise, cross-correlation (Shapiro & Campillo, 2004; Stehly et al., 2006) and cross-coherence (Aki, 1957; Combs, 1978; Schuster et al., 2003; Nakata et al., 2011). Alternative approaches include deconvolution (Vasconcelos & Snieder, 2008a, 2008b; Snieder et al., 2009) and multi-dimensional deconvolution (Wapenaar et al., 2008, 2011; Van Dalen et al., 2015; Weemstra et al., 2016; Cheng et al., 2017), both of which have been utilized for seismic interferometry. In general, generation of EGF's using cross-correlation is the simplest and currently most popular technique with numerous examples of successful field application. The cross-coherence algorithm is also referred to as whiten cross-correlation; Prieto et al. (2009) demonstrates performing cross-correlation with spectral whitening is equivalent to calculating the cross-coherence. However, the choice of spectral whitening approach and the corresponding parameters can yield differences in the extracted EGFs. Figure.4 presents a comparison between cross-correlation and cross-coherence with the same preprocessed noise waveforms. We observe distinct pseudo-arrivals existing on extracted cross-correlation functions (Fig.4a and Fig.4b). These may be caused by insufficient spectral normalization during the data preprocessing procedure. Figure.4c shows the spectral difference between the averaged cross-correlation functions and the cross-coherence functions; several distinct spikes observed in the cross-correlation functions have been significantly attenuated after the further spectral normalization included in the cross-coherence algorithm. These kinds of pseudo-arrivals are almost inevitable since selection of the appropriate data preprocessing workflow requires substantial manual tuning. However, the existence of the pseudo-arrivals could mislead interpreters, particularly for coda wave interferometry, since they could be mistaken for coda waves while not encoding any subsurface information. In fact, they only reflect the seismic signatures associated with some specific sources, for example, the narrow-band persistent source signatures observed on the spectrograms (indicated by the double arrow on Fig.2b) with peak frequencies around 3, 4.2, 5.5, 7.5 Hz which are consistent with the spikes presenting on the cross-correlation spectrum (Fig.4c). Therefore, we recommend the use of cross-coherence for ambient noise interferometry. With pseudo-arrivals removal, the cross-coherence functions show much cleaner virtual-source gather (see Fig.S1 in the supporting information) with higher signal to noise ratio (SNR) (see Fig.S2 in the supporting information).

3.3 Surface Waves and Body Waves

Due to limitation from the single-component instrument as well as the poor data quality on horizontal components, most ambient noise interferometry studies focus primarily on the vertical component, accounting for Rayleigh waves retrieval, even with months- or years- duration time observations (Lehujeur et al., 2018; Martins et al., 2019; Planès et al., 2020). In order to go beyond the retrieval of Rayleigh waves from ambient noise interferometry, we apply cross-coherence on both vertical component (Z-Z) and horizontal components (NN, EE, NE, EN). After cross-coherence, we employ phase-weighted stacking on the 4.7 days cross-coherence functions to further improve the coherence signals (Schimmel & Paulssen, 1997; Schimmel et al., 2011; Ventosa et al., 2017), and rotate the north and east horizontal components into radial (R) and transverse (T) components (Lin et al., 2008). Finally, we obtain $3 * C_N^2 = 3 * 18336$ high quality cross-coherence functions for Z-Z, R-R and T-T components.

Figure.5 presents the bin-stacked cross-coherence gathers from Z-Z (a), R-R (b) and T-T (c) components by stacking all available interstation cross-coherence pairs in a 70m offset bin. A bandpass filter between 1 and 10Hz has been applied for better display. Clear Rayleigh waves with apparent velocity around 2.5 km/s can be observed on both Z-Z and R-R components; high quality Love waves with slightly higher apparent velocity around 2.7 km/s are also distinct on the T-T component. Moreover, we can also distinguish body waves with apparent velocity around 4.2 km/s on the whole offset range of R-R component (highlighted on Fig.5b), as well as on the near-offset (<2 km) sections of Z-Z and T-T components.

We applied dispersion analysis on the bin-stacked virtual-sources gathers by using a frequency-domain slant-stacking technique that has been frequently utilized for multi-channel analysis of surface wave (MASW Park et al., 1998). For clearer presentation, all dispersion images in this work have been normalized along the frequency direction. Figure.6

displays the obtained dispersion spectra from Z-Z (a), R-R (b) and T-T (c) components. A clear dispersive energy trend can be observed for Rayleigh waves on Figure.6a and Figure.6b, and Love waves on Figure.6c. We are able to pick continuous dispersion curves from 1Hz to 10Hz for both Rayleigh and Love wave, and the picked dispersion curves (see Fig.S3 in the supporting information) can be taken as reference for later two-station surface wave dispersion analysis.

Compared with the surface wave dispersion energy, the non-dispersive energy trend with higher frequencies and higher velocities suggests the presence of body waves. It is in good agreement with the observation of the high frequency higher velocity (>4 km/s) beam energy seen in our previous beamforming analysis (Fig.3). Both virtual-sources gathers (Fig.5) and dispersion spectra (Fig.6) illustrate that the body-wave energy is dominant on the radial (R-R) component. For typical velocity structures (e.g. velocity increasing with depth), P-waves at larger offsets should be stronger on the vertical component due to the bending of the upcoming waves towards the vertical. However, a sonic log from the center of the area (see Fig.S4 in the supporting information) indicates the existence of a thin hard (high-velocity) surface layer, resulting in a significant velocity decrease with depth. Consequently, upcoming waves will be bent away from the vertical, and P-wave energy can be strong on the radial component. We use the ray tracing code ANRAY (Gajewski & Pšencík, 1987; Gajewski & Psencik, 1989) to model travel times and amplitudes based on the 1D velocity model from the sonic log. It shows that the shallow high-velocity layer leads to significant bending of the raypath (Fig.7a), and that the presumed body-wave moveout in virtual source gathers fits well with the calculated travel times (Fig.7b). The radial component of the modeled P-wave amplitudes is significantly stronger than the vertical component (Fig.7c), confirming the assumption of observation of P-wave energy on the radial component of the interferograms. These observations suggest that double-beamforming techniques might be useful for isolating the body wave energy from the ambient noise field and enhancing P first arrivals for body wave tomography (Nakata et al., 2016; Castellanos et al., 2020).

3.4 Phase Velocity Dispersion Measurement

Recent ambient noise tomography applications for geothermal reservoir imaging focus on measurement of Rayleigh wave group velocities (Lehujeur et al., 2016, 2018; Planès et al., 2020), probably because of the directivity bias on phase velocity estimation from the inhomogeneous source distribution (Lin et al., 2008). However, the phase velocity measurements have the advantages of less uncertainly and higher depth sensitivity over the group velocity measurements. Based on the beamforming analysis and the perfect symmetry between the negative and positive time lags of the obtained interferograms, we believe the source distribution in Andi town is able to provide sufficient illumination for complete EGFs retrieval as well as dispersion measurements, at least for the frequency band between 1Hz and 10Hz.

We employ the an image transformation technique introduced by Yao et al. (2006) for phase velocity estimation based on the extracted EGFs. Considering the higher quality of the retrieved Rayleigh waves on Z-Z component over that on R-R component (see Fig.S5 in the supporting information), we choose the Z-Z component EGFs for Rayleigh waves phase velocity estimation. The T-T component EGFs are used for Love waves phase velocity estimation.

In order to ensure the quality of dispersion measurements, we set a series of criteria for quality control:

1. we reject interstation pairs with distance <0.6 km to avoid the potential near-field effects on the dispersion measurement (Yoon & Rix, 2009; Foti et al., 2018);

2. we reject EGFs with SNR < 7 although most of EGFs show SNR > 10 (see Fig.S5 in the supporting information);
3. we apply velocity filter on extracted EGFs and mute arrivals beyond the velocity band from 1.5 km/s to 3.5 km/s considering the local velocity range;
4. we set the interstation distance has to be longer than 1.5 times wavelength;
5. we limit the frequency band of dispersion curves above 1Hz to ensure the appropriate illumination.

As for the wavelength criterion, it usually varies with the data as well as the necessaries change. Bensen et al. (2007) suggests a strict criterion with 3 times wavelength accounting for the far-field approximation; others choose a criterion with 1.5 times wavelength (e.g., Mordret et al., 2015; Obermann et al., 2016; Fallahi et al., 2017); Luo et al. (2015) demonstrates that one wavelength is still consistent with and also reliable as these with stricter wavelength criterion. In this work, we choose the 1.5 times wavelength criterion in order to get rid of the potential directional noise effects although our high quality EGFs allow us to go beyond the 1.5 times wavelength.

Figure.8 displays examples of dispersion analysis on extracted Rayleigh and Love wave by using the an image transformation technique. The red waveforms present the velocity filtered EGFs used for Rayleigh and Love wave dispersion measurements, separately. Clear fundamental modes can be observed on the obtained dispersion spectra. The spectral energy besides the fundamental modes indicates the 2π ambiguity caused by phase velocity measurement (Yao et al., 2006). We overly the dispersion spectra with the averaged dispersion curves picked from the bin-stacked virtual-source gathers for reference. The blue dash lines indicate the 1.5 times wavelength criterion.

3.5 Dispersion Curves Picking using Machine Learning

After dispersion measurements for both Rayleigh and Love waves, noisy dispersion images are manually rejected by visual inspection. Finally, a task pool with more than 23k dispersion measurements is prepared for dispersion curves picking. We utilize a deep learning model, named DCNet developed by Dai et al. (2020), for full automatic dispersion curve picking by regrading dispersion curves extracted as an instance segmentation task. To help the machine to distinguish the target dispersion curves in this work, we set a confidence region based on the reference dispersion curves picked from the bin-stacked virtual-source gathers. First, we smooth the reference dispersion curves v_{ref} by linear regression; next, we build the upper and bottom boundaries of the confidence region with an extreme 25% velocity variation, $v_{upper} = 1.25 * v_{ref}$ and $v_{bottom} = 0.75 * v_{ref}$. The dispersion spectra beyond the confidence region has masked. We manually pick 1% dispersion curves which are randomly selected from the task pool, and the high cross-correlation (95.32%) between the manually picked dispersion curves and the ML picked dispersion curves indicates the high quality of the automatically dispersion curves picking.

Figure.9 shows examples of dispersion curves picking by using the Machine Learning (ML) technique. The excellent match between the ML picked dispersion curves (the cyan curves) and the manually picked dispersion curves (the magenta curves) demonstrates the accuracy of the ML picks. Figure.10 presents all the automatically picked dispersion curves for Rayleigh waves (a) and Love waves (b) between 1 and 10Hz. The magenta curves indicate the smoothed reference dispersion curves, and the green dash lines highlight the confidence region defined by the smoothed reference dispersion curves. Filtered by a series of quality control criteria, we obtain 12,593 fundamental dispersion curves for Rayleigh waves and 11,105 fundamental dispersion curves for Love waves from $2 * C_N^2 = 2 * 18336$ EGFs, with a data utilization coefficient of 64.6%. See Fig.S6 for the distribution of the interstation distance as well as SNR for the picked dispersion curves in the supporting information.

3.6 Surface Wave Tomography

Based on the picked dispersion curves for both Rayleigh waves and Love waves, we construct two-dimensional (2-D) phase velocity distribution maps for a series of frequencies from 1Hz to 10Hz using a non-linear 2-D tomographic inversion technique (Rawlinson, 2005; Rawlinson & Sambridge, 2005). The inversion algorithm includes an eikonal solver based on the fast marching method (FMM, Rawlinson & Sambridge, 2005) for ray tracking and a subspace inversion scheme for the iterative inversion steps (Kennett et al., 1988). It accounts for propagation effects caused by rapid changes in the velocity field, and allows both smoothing and damping regularization to be imposed in order to address the problem of solution non-uniqueness. To tune the value of the two regularization parameters, we apply the L-curve approach (Hansen, 1992) to coordinate the traveltime misfit and model variance as well as model roughness and define the optimal parameters.

An adequate model resolution can help to identify subsurface anomalies' geometries, which is relevant for subsurface characteristics and geothermal purposes. We employ checkerboard sensitivity tests (Lévěque et al., 1993) to check the ability of the inversion algorithm to reconstruct structure at different locations in model space. Based on the picked dispersion curves, a background velocity of 2.5 km/s with $\pm 10\%$ perturbations has been targeted for forward modeling. Since in our case Rayleigh waves picks have a better raypath distribution compared with Love waves (see Fig.S7 and Fig.S8 in the supporting information), we check the geometry limitation as well as spatial resolution based on the Love wave observations. A series of checkerboard with different spatial resolutions ranging from 0.1 km to 0.5 km have been reproduced for each frequency because the numbers and spatial densities of the raypaths vary with frequencies. Figure.11 presents the simulated checkerboard models and tomographic results with two different grid sizes, 0.3 km (left panels) and 0.2 km (right panels). A series of simulated tests demonstrate that the inversion should allow us to estimate a spatial resolution of around 0.2km$\sim$0.3km with higher resolution in the center of our seismic network and lower resolution towards the border of our investigation area. We define a resolved zone with the raypath density of Love wave (see Fig.S7 in the supporting information) greater than 60 per 0.3x0.3km^2 cell grid at median frequency 5.0Hz where the simulated tests with grid sizes of both 0.3 km and 0.2 km can be well recovered, as indicated by the black curves on Figure.11. Note that the resolved zone has been smoothed for spatial consistency. Pixels outside the resolved zone are masked in the final maps.

Figure.12 presents the tomographic inversion results at 1.4Hz, 6.0Hz and 9.8Hz for both Rayleigh waves (the left panels) and Love waves (the right panels). The black contour plotted on each map delineates the resolved zone defined by the raypath density. Any features outside this contour should be interpreted with caution. Broadly, the average velocity obtained decreases with the frequency (see the reference velocity in the subplot titles); the relative phase velocity variations of Rayleigh and Love waves exhibit similar patterns for all frequencies with lower velocities in the north and higher velocities at south. The histograms of traveltime residuals have small standard deviations indicating good coherence between the measurements, on average (see Fig.S9 in the supporting information).

4 Results

4.1 Three-dimensional S wave velocity

To build a high-resolution 3-D S wave velocity model of the area, we jointly invert the Rayleigh and Love wave dispersion curves obtained in each pixel of the tomographic inversions (Fig.12) by using a neighborhood algorithm (NA) with a Monte Carlo solver, Geopsy (Wathelet et al., 2004). Compared with single wave type dispersion inversion, joint inversion of both Rayleigh and Love wave has the advantages of reducing non-uniqueness inherent in surface-wave methods and improving the accuracy of the inverted S wave velocity model (Joh et al., 2006; Chmiel et al., 2019; Yin et al., 2020). The 1-D depth model is parameterized with 13 layers including a half-space at the bottom (Table.1). The density parameter is gradually increased with the depth based on borehole observations; Vp is linked to Vs during the inversion with a dynamic Poisson ratio range from 0.2 to 0.5; a loose prior constraint, based on the empirical formula on Xia et al. (1999), is applied to Vs. For each location, we invert the obtained dispersion curves with 3 runs of the inversion process. Each run retains 2500 models and we end up with the best 500 models from all 3 runs. Figure.13 presents an example of the 1-D depth inversion. The forward modeled dispersion curves simultaneously converge to the measured Rayleigh (Fig.13a) and Love (Fig.13b) data with very small misfits. Although surface wave phase velocity is less sensitive to Vp compared to Vs, the coherence of both inverted Vs (Fig.13d) and Vp models (Fig.13d) still indicates a stable inversion processing.

We run 1-D depth inversions independently for each pixel (151x139) on the tomographic maps, and combine the optimum 1-D Vs model obtained at each pixel to form a 3-D Vs model. Figure.14 presents the inverted Vs maps at depths of 0.10 km, 0.48 km, 0.90 km, 1.22 km, 1.64 km, and 2.20 km. The primary pattern that emerges from both the tomographic phase velocity maps and the inverted Vs maps is the negative velocity variations at north, which corresponds to the young Jurassic sediments, and the positive velocity variations at south, which corresponds to the coarse-grained adamellites in the mountain areas. The negative velocity anomalies along the north river channel (the gray lines on Fig.14) also coincide with the alluvial deposits from the Quaternary system; we can observe similar anomalies across the CSAMT line (the black lines on Fig.14) at shallower depths. It is worth noting that the small negative velocity anomalies ($< 3\%$) in the southwestern water reservoir area (outlined by the green lines on Fig.14) could be artifacts caused by the influence from the water reservoir on the surface wave raypaths. Figure.15 shows variable performances of the sensitivity kernels between Rayleigh and Love wave for the 1-D velocity model at the well location (the magenta crosses on Fig.14). Joint analysis of Rayleigh and Love wave offers a multiple-scale vertical resolution investigation result from surface to depth 2 km.

4.2 HVSR Measurement

Most ambient noise studies only focus on extraction of the phase information for travel time tomography but abandon the amplitude information. Ambient noise (microtremors) horizontal-to-vertical spectral ratio (HVSR) provides the opportunity to extend the ambient noise studies beyond the phase extraction scope, since multiple-component sensing has been more and more regular for seismic data acquisition. HVSR method has been widely used for estimation of predominant vibration frequency of soils, mainly for microzonation and site effect purposes (Acerra et al., 2004; Gosar et al., 2010; Leyton et al., 2013; García-Jerez et al., 2016, 2019). Although the theoretical basis of the HVSR method is still debated, HVSR has been widely accepted as related to the ellipticity of Rayleigh waves and frequency dependent (Bard et al., 1999; Sylvette et al., 2006). Therefore, HVSR exhibits a sharp peak at the fundamental frequency of the sediments, when there is a high impedance contrast between the sediments and underlying bedrock.

Following spectral analysis on the raw waveforms as described above, we apply Konno-Ohmachi smoothing (Konno & Ohmachi, 1998) with a b value of 40 on each one-hour averaged PSD spectrogram for 3 components of all available stations. Next, we calculate the HVSR as the square root of the ratio of the spectral energy components:

$$\frac{H}{V}(x,w) = \sqrt{\frac{E_1(x,w) + E_2(x,w)}{E_3(x,w)}}, \tag{1}$$

where, E_1 and E_2 stand for the spectral energy for the horizontal components; E_3 stands for the spectral energy for the vertical component; x indicates the station location; w

is the angular frequency. The spectral energy can also be computed from the average autocorrelation of the ambient noise wavefield (Perton et al., 2018). Finally, we obtain over 100 one-hour averaged HVSR functions from 4.7 days observation, and the average HVSR function of all windows is taken as the final HVSR measurement of the corresponding location. We estimate the measurement precision for each frequency by 0.6 times of the standard deviation.

Figure.16 presents two examples of the obtained HVSR measurements from stations located at north (a) and south (b), separately. A clear peak with large amplitude (> 3) (Fig.16a) is related to a high impedance contrast between the sedimentary cover and the basement while a low amplitude (< 3) (Fig.16b) usually indicates a lower contrast, for example of the presence of a hard soil at rock sites (Bard et al., 1999; Woolery & Street, 2002; Bonnefoy-Claudet et al., 2006, 2008). The peak frequency (f_0), or natural frequency, from HVSR measurement also reflects the sediment depth (h) with a general relationship $f_0 = \frac{V_s}{4h}$ (Castellaro & Mulargia, 2009; Pazzi et al., 2017). We reject the HVSR measurements (24/192) with flat HVSR curves and amplitudes smaller than 1 (see Fig.S10 in the supporting information) according to Acerra et al. (2004).

Figure.17a displays all available HVSR measurements overlaying on the surface geology map (Fig.1b). We cluster the HVSR peaks based on the peak frequencies coded by the colors as well as the peak values coded by the scales. We observe four primary units that strongly correlate with the background geology:

1. to the north part of the area, large (>4) and dark blue (<8Hz) HVSR peaks indicate the strong impedance contrast between the thick sediment and the basement, which is colocated with the younger Jurassic sediment;
2. to the south of the area, small (<2) and dark red (>11Hz) HVSR peaks indicate the weak contrast between the hard rock surface, where coarse-grained adamellites are widely distributed, and the basement;
3. along the river crossing the town, medium size HVSR peaks with peak frequencies around 9Hz coincide with the fluvial deposits from the Quaternary system;
4. in the central area, a transition zone with various peak frequencies and peak values HVSR measurements is highlighted by the magenta shadow belt.

Figure.17b presents the iso-surface of the median velocity of the inverted Vs model with Vs = 3.0km/s. The surface colors are coded by depths. Although it does not strictly reflect the basement surface, the northern cavern and the southern hump indicate the rather deeper basement in the north than that in the south. These results are consistent with HVSR observations with the lower peak frequencies distributed in the north and higher peak frequencies distributed in the south. The lower surface velocities in the north (Fig.14a) coincide with the stronger impedance contrast inferred from the larger HVSR peaks.

5 Discussion

We successfully resolve 3-D S wave velocity model from the surface to 2 km depth with spatial resolutions of 0.2 km∼0.3 km, and observe the negative velocity variation around 3% to depths of up to 1 km in the fluvial deposit area. These low-velocity anomalies are consistently present at depth in both frequency (Fig.12) and depth (Fig.14) domains. The transition belt observed on HVSR measurements also covers this area. These lower velocity anomalies may be associated with the high-temperature geothermal field from deep to surface. The cross sections of the S wave velocity structure as well as the electric resistivity measurement in Figure.18 provide additional insight on the spatial distribution of the potential geothermal filed.

Vertical cross sections along the CSAMT profile line present clear velocity anomalies from both the absolute velocity profile (Fig.18a) and the velocity variation (Fig.18b) profile. In particular, distinct low velocity anomalies can be observed on the velocity variation profile from location 1.0 km to location 1.6 km. We are able to infer three steep faults, Fw^1, Fw^2 and Fw^3, based on the boundary of the positive and negative velocity variation. Fw^3 has been proven by the surface geology observation. The low velocity anomalies among Fw^1 and Fw^2 appear as a channel from deep to surface, which is consistent with the colocated conductive region on the resistivity profile, which is suggested as hot flow signature. Note that we mask the two sides of the cross sections that beyond the resolvable zone.

Figure.19 presents the 3-D view of the iso-surfaces of the velocity variations at ΔV = -3% (a) and ΔV = -1% (b). The surface colors are coded by depths. The horizontal slice shows the plane Vs variation at depth 2.0 km. The slice colors are coded by the velocity variations as Figure.14. The resolvable zone is indicated by the black line. We observe a clear reservoir bounded by the negative velocity anomalies surface on Figure.19a, which is colocated with the observed transition belt on HVSR measurements. However, we are not going to further discuss the anomalies beyond the resolvable zone since they could be potentially stretched during the tomography due the poor resolve resolution. Within the resolvable zone, a funnel-shaped low-velocity zone (LVZ) (indicated by the green arrow) is visible on Figure.19a. It biases from south to north with the depth increasing, and the root turns to be broader with velocity variation decreasing to ΔV = -1% (Fig.19b). The CSAMT profile (indicated by the white line) intersects this LVZ particularly the smaller velocity variation surface on Figure.19b. Combined with the conductive characteristics observed on CSAMT profile, we interpret this LVZ as a zone of more intense fracturing with conductive fluids (Guéguen & Palciauskas, 1994; Paterson & Wong, 2005; Lehujeur et al., 2018). We also observe the drilling well (indicated by the thick black stick on Fig.19b) crossing into the LVZ from depth around 1 km, which has been proven by the sudden decrease around 1 km in fluid resistivity well records (the black curve on Fig.20). The sudden decrease in fluid resistivity also supports our interpretation that the fluid filled fracture channel presents as a more conductive zone than the surrounding rocks. The gradually increasing borehole temperature logs (the magenta curve on Fig.20a) show a gradient of around $3^oC/100$m indicating the existence of the higher-temperature geothermal resources at depth.

We also observe a columnar LVZ (indicated by the blue arrow) on Figure.19b which is located beneath the water reservoir. As described above, this abnormal body could be artifacts caused by the influence from the water reservoir on the surface wave ray-paths. Another shallow (above 0.9 km) abnormal body is indicated by the red arrow on Figure.19b. We cannot rule out the possibility that the observed shallow anomalies are related with the geothermal activity. Unlike the LVZ indicated by the green arrow, however, this one loses the surface water resource from the nearby Plum Creek River which might limit the condition for the generation of a good geothermal field since the underground water layer in this area is usually deeper than the maximum depth of the abnormal body. Both questions could be addressed if we can include more constraints, for example extraction body wave from interferograms for traveltime tomography or application of additional magnetotelluric (MT) surveys.

6 Conclusions

We successfully retrieve surface waves, both Rayleigh and Love waves, from ambient noise over an ultra-short observation period using a dense nodal array, and apply tomographic imaging of the subsurface 2 km S wave velocity structure beneath a rural town. For the first time, we demonstrate the advantage of cross-coherence over cross-correlation on suppressing pseudo-arrivals cased by persistent sources. Body waves are also observed on the cross-coherence functions which offer the possibility for the further body wave tomography study. We investigate spatial horizontal resolutions for the tomographic inversion and present a resolvable zone with the highest resolution of 0.2 km. Strong correlation between HVSR measurements and S wave velocity model indicates the potential of extraction of both amplitude and phase information from 3C ambient noise data, which will increase the data utilization coefficient and provide more constraints for ambient noise imaging. Given the continually increasing demands for the development of local geothermal resources, particularly in China, our work demonstrates the utility of high spatial-resolution geothermal characterization with affordable seismic nodal array observation, as well as high temporal-resolution geothermal monitoring due to the ultra-short observation period.

We detect low-velocity anomalies (between -1% and -4%) from surface to depth in the central area, which is inferred as a fracture channel filled in with the fluid contents in the light of observation of the colocated conductive zone on resistivity profile. Joint interpretation based on HVSR measurements, the temperature and fluid resistivity records observed in a nearby well suggests the existence of the high-temperature geothermal field through the fracture channel.

Acknowledgments

This study is supported by the National Natural Science Foundation of China under grant No. 41830103 and Zhejiang Geophysical and Geochemical Prospecting Academy. The seismic time-series datasets utilized in this paper were archived in the Mendeley Data (`http://dx.doi.org/10.17632/382frvcy6r.3`). We appreciate Dr. Shucheng Wu for many useful suggestions on surface wave tomography.

References

Acerra, C., Havenith, H.-B., & Zacharopoulos, S. (2004). *Guidelines for the implementation of the h/v spectral ratio technique on ambient vibrations measurements, processing and interpretation* (Tech. Rep.). European Commission.

Aki, K. (1957). Space and time spectra of stationary stochastic waves, with special reference to microtremors. *Bulletin of the Earthquake Research Institute*, *35*, 415–456.

Ali, M. Y., Barkat, B., Berteussen, K. A., & Small, J. (2013). A low-frequency passive seismic array experiment over an onshore oil field in Abu Dhabi , United Arab Emirates. *Geophysics*, *78*(4), B159–B176.

Ardhuin, F., Gualtieri, L., & Stutzmann, E. (2015). How ocean waves rock the earth: Two mechanisms explain microseisms with periods 3 to 300 s. *Geophysical Research Letters*, *42*(3), 765–772.

Atef, H., Abd El-Gawad, A., Zaher, M. A., & Farag, K. (2016). The contribution of gravity method in geothermal exploration of southern part of the gulf of suez–sinai region, egypt. *NRIAG Journal of Astronomy and Geophysics*, *5*(1), 173–185.

Bakulin, A., & Calvert, R. (2006). The virtual source method: Theory and case study. *Geophysics*, *71*(4), 139–150.

Bard, P.-Y., et al. (1999). Microtremor measurements: a tool for site effect estimation. *The Effects of Surface Geology on Seismic Motion*, *3*, 1251–1279.

Behm, M., Cheng, F., Patterson, A., & Soreghan, G. (2019). Passive processing of active nodal seismic data: Estimation of Vp/Vs ratios to characterize structure and hydrology of an alpine valley infill. *Solid Earth*, 1–32. doi: 10.5194/se-2019-47

Behm, M., Leahy, G. M., & Snieder, R. (2014). Retrieval of local surface wave velocities from traffic noise - an example from the La Barge basin (Wyoming). *Geophysical Prospecting*, *62*(2), 223–243.

Bensen, G., Ritzwoller, M., Barmin, M., Levshin, A., Lin, F., Moschetti, M., . . .

Yang, Y. (2007). Processing seismic ambient noise data to obtain reliable broad-band surface wave dispersion measurements. *Geophysical Journal International*, *169*, 1239–1260.
Bonnefoy-Claudet, S., Cornou, C., Bard, P.-Y., Cotton, F., Moczo, P., Kristek, J., & Donat, F. (2006). H/v ratio: a tool for site effects evaluation. results from 1-d noise simulations. *Geophysical Journal International*, *167*(2), 827–837.
Bonnefoy-Claudet, S., Köhler, A., Cornou, C., Wathelet, M., & Bard, P.-Y. (2008). Effects of love waves on microtremor h/v ratio. *Bulletin of the Seismological Society of America*, *98*(1), 288–300.
Campillo, M., & Paul, A. (2003). Long-range correlations in the diffuse seismic coda. *Science*, *299*(5606), 547–549.
Castellanos, J. C., Clayton, R. W., & Juarez, A. (2020). Using a time-based subarray method to extract and invert noise-derived body waves at long beach, california. *Journal of Geophysical Research: Solid Earth*, *125*(5), e2019JB018855.
Castellaro, S., & Mulargia, F. (2009). Vs30 estimates using constrained h/v measurements. *Bulletin of the Seismological Society of America*, *99*(2A), 761–773.
Cheng, F., Draganov, D., Xia, J., Behm, M., & Hu, Y. (2017). Deblurring directional-source effects for passive surface-wave surveys using multidimensional deconvolution. *AGUFM*, *2017*, S21C–0736.
Cheng, F., Xia, J., Behm, M., Hu, Y., & Pang, J. (2019). Automated Data Selection in the Tau–p Domain: Application to Passive Surface Wave Imaging. *Surveys in Geophysics*, 1–18. doi: 10.1007/s10712-019-09530-2
Cheng, F., Xia, J., Luo, Y., Xu, Z., Wang, L., Shen, C., ... Hu, Y. (2016). Multichannel analysis of passive surface waves based on cross-correlations. *Geophysics*, *81*(5), EN57–EN66.
Cheng, F., Xia, J., Xu, Y., Xu, Z., & Pan, Y. (2015). A new passive seismic method based on seismic interferometry and multichannel analysis of surface waves. *Journal of Applied Geophysics*, *117*, 126–135.
Cheng, F., Xia, J., Xu, Z., Hu, Y., & Mi, B. (2018). Frequency – Wavenumber (FK)- Based Data Selection in High - Frequency Passive Surface Wave Survey. *Surveys in Geophysics*, *39*, 661–682.
Chmiel, M., Mordret, A., Boué, P., Brenguier, F., Lecocq, T., Courbis, R., ... Van der Veen, W. (2019). Ambient noise multimode rayleigh and love wave tomography to determine the shear velocity structure above the groningen gas field. *Geophysical Journal International*, *218*(3), 1781–1795.
Combs, J. (1978). *Geothermal exploration techniques: a case study. final report.[coso geothermal area]* (Tech. Rep.). Texas Univ., Richardson (USA). Center for Energy Studies.
Combs, J., & Hadley, D. (1977). Microearthquake investigation of the mesa geothermal anomaly, imperial valley, california. *Geophysics*, *42*(1), 17–33.
Dai, T., Xia, J., Ning, L., Xi, C., Liu, Y., & Xing, H. (2020). Deep learning for extracting dispersion curves. *Surveys in Geophysics*, 1–27.
Dean, T. (2017). The seismic signature of rain. *Geophysics*, *82*(5), P53–P60. doi: 10.1190/geo2016-0421.1
Draganov, D., Campman, X., Thorbecke, J., Verdel, A., & Wapenaar, K. (2009). Reflection images from ambient seismic noise. *Geophysics*, *74*(5), A63–A67.
Fallahi, M. J., Obermann, A., Lupi, M., Karyono, K., & Mazzini, A. (2017). The plumbing system feeding the lusi eruption revealed by ambient noise tomography. *Journal of Geophysical Research: Solid Earth*, *122*(10), 8200–8213.
Foti, S., Hollender, F., Garofalo, F., Albarello, D., Asten, M., Bard, P.-Y., ... others (2018). Guidelines for the good practice of surface wave analysis: A product of the interpacific project. *Bulletin of Earthquake Engineering*, *16*(6), 2367–2420.
Gajewski, D., & Pšencík, I. (1987). Computation of high-frequency seismic wavefields in 3-d laterally inhomogeneous anisotropic media. *Geophysical Journal*

International, *91*(2), 383–411.
Gajewski, D., & Psencik, I. (1989). Ray synthetic seismograms in 3-d laterally inhomogeneous anisotropic structures-program anray89. *LBL Center for Computational Seismology, Berkeley, CA*.
Ganguly, S., & Kumar, M. M. (2012). Geothermal reservoirs—a brief review. *Journal of the Geological Society of India*, *79*(6), 589–602.
García-Jerez, A., Piña-Flores, J., Sánchez-Sesma, F. J., Luzón, F., & Perton, M. (2016). A computer code for forward calculation and inversion of the H/V spectral ratio under the diffuse field assumption. *Computers and Geosciences*, *97*, 67–78. doi: 10.1016/j.cageo.2016.06.016
García-Jerez, A., Seivane, H., Navarro, M., Martínez-Segura, M., & Piña-Flores, J. (2019). Joint analysis of Rayleigh-wave dispersion curves and diffuse-field HVSR for site characterization: The case of El Ejido town (SE Spain). *Soil Dynamics and Earthquake Engineering*, *121*, 102–120. doi: 10.1016/j.soildyn.2019.02.023
Gerstoft, P., & Tanimoto, T. (2007). A year of microseisms in southern california. *Geophysical Research Letters*, *34*(20).
Gosar, A., Rošer, J., Šket Motnikar, B., & Zupančič, P. (2010). Microtremor study of site effects and soil-structure resonance in the city of Ljubljana (central Slovenia). *Bulletin of Earthquake Engineering*, *8*(3), 571–592. doi: 10.1007/s10518-009-9113-x
Groos, J., & Ritter, J. (2009). Time domain classification and quantification of seismic noise in an urban environment. *Geophysical Journal International*, *179*(2), 1213–1231.
Guéguen, Y., & Palciauskas, V. (1994). *Introduction to the physics of rocks*. Princeton University Press.
Hansen, P. C. (1992). Analysis of discrete ill-posed problems by means of the l-curve. *SIAM review*, *34*(4), 561–580.
Hochstein, M. P., & Soengkono, S. (1997). Magnetic anomalies associated with high temperature reservoirs in the taupo volcanic zone (new zealand). *Geothermics*, *26*(1), 1–24.
Hu, S., & Wang, J. (2000). Heat flow, deep temperature and thermal structure across the orogenic belts in southeast china. *Journal of Geodynamics*, *30*(4), 461–473.
Joh, S.-H., Stokoe, K. H., II, Lee, I.-W., Kang, T.-H., Rosenbld, B., & Bay, J. A. (2006). Joint inversion for apparent phase velocities of rayleigh and love waves. In *Geocongress 2006: Geotechnical engineering in the information technology age* (pp. 1–6).
Keller, G. (1981). Exploration for geothermal energy. In *Developments in geophysical exploration methods* (pp. 107–149). Springer.
Kennett, B., Sambridge, M., & Williamson, P. (1988). Subspace methods for large inverse problems with multiple parameter classes. *Geophysical Journal International*, *94*(2), 237–247.
Konno, K., & Ohmachi, T. (1998). Ground-motion characteristics estimated from spectral ratio between horizontal and vertical components of microtremor. *Bulletin of the Seismological Society of America*, *88*(1), 228–241.
Lacoss, R. T., Kelly, E. J., & Toksöz, M. N. (1969). Estimation of seismic noise structure using arrays. *Geophysics*, *34*(1), 21–38.
Lehujeur, M., Vergne, J., Maggi, A., & Schmittbuhl, J. (2016). Ambient noise tomography with non-uniform noise sources and low aperture networks: case study of deep geothermal reservoirs in northern alsace, france. *Geophysical Supplements to the Monthly Notices of the Royal Astronomical Society*, *208*(1), 193–210.
Lehujeur, M., Vergne, J., Schmittbuhl, J., Zigone, D., Le Chenadec, A., & Team, E. (2018). Reservoir imaging using ambient noise correlation from a dense seismic

network. *Journal of Geophysical Research: Solid Earth*, *123*(8), 6671–6686.

Lévěque, J.-J., Rivera, L., & Wittlinger, G. (1993). On the use of the checker-board test to assess the resolution of tomographic inversions. *Geophysical Journal International*, *115*(1), 313–318.

Leyton, F., Ruiz, S., Sepúlveda, S. A., Contreras, J. P., Rebolledo, S., & Astroza, M. (2013). Microtremors' HVSR and its correlation with surface geology and damage observed after the 2010 Maule earthquake (Mw 8.8) at Talca and Curicó, Central Chile. *Engineering Geology*, *161*, 26–33. doi: 10.1016/j.enggeo.2013.04.009

Lin, F.-C., Moschetti, M. P., & Ritzwoller, M. H. (2008). Surface wave tomography of the western united states from ambient seismic noise: Rayleigh and love wave phase velocity maps. *Geophysical Journal International*, *173*(1), 281–298.

Lin, F.-C., Ritzwoller, M. H., & Snieder, R. (2009). Eikonal tomography: surface wave tomography by phase front tracking across a regional broad-band seismic array. *Geophysical Journal International*, *177*(3), 1091–1110.

Liu, Y., Wang, G., Zhu, X., & Li, T. (2019). Occurrence of geothermal resources and prospects for exploration and development in china. *Energy Exploration & Exploitation*, 0144598719895820.

Long, H., Zhu, Q., Tian, P., & Hu, W. (2015). Technologies and applications of geophysical exploration in deep geothermal resources in china. In *Proceedings of the world geothermal congress.*

Luo, Y., Yang, Y., Xu, Y., Xu, H., Zhao, K., & Wang, K. (2015). On the limitations of interstation distances in ambient noise tomography. *Geophysical Journal International*, *201*(2), 652–661. doi: 10.1093/gji/ggv043

Lüschen, E., Dussel, M., Thomas, R., & Schulz, R. (2011). 3d seismic survey for geothermal exploration at unterhaching, munich, germany. *First Break*, *29*(1).

Martins, J. E., Ruigrok, E., Draganov, D., Hooper, A., Hanssen, R., White, R., & Soosalu, H. (2019). Imaging torfajökull's magmatic plumbing system with seismic interferometry and phase velocity surface wave tomography. *Journal of Geophysical Research: Solid Earth*, *124*(3), 2920–2940.

Martins, J. E., Weemstra, C., Ruigrok, E., Verdel, A., Jousset, P., & Hersir, G. (2020). 3d s-wave velocity imaging of reykjanes peninsula high-enthalpy geothermal fields with ambient-noise tomography. *Journal of Volcanology and Geothermal Research*, *391*, 106685.

McNamara, D. E., & Buland, R. P. (2004). Ambient noise levels in the continental united states. *Bulletin of the seismological society of America*, *94*(4), 1517–1527.

Mordret, A., Rivet, D., Landès, M., & Shapiro, N. M. (2015). Three-dimensional shear velocity anisotropic model of piton de la fournaise volcano (la réunion island) from ambient seismic noise. *Journal of Geophysical Research: Solid Earth*, *120*(1), 406–427.

Munoz, G. (2014). Exploring for geothermal resources with electromagnetic methods. *Surveys in geophysics*, *35*(1), 101–122.

Nakata, N., Boué, P., Brenguier, F., Roux, P., Ferrazzini, V., & Campillo, M. (2016). Body and surface wave reconstruction from seismic noise correlations between arrays at piton de la fournaise volcano. *Geophysical Research Letters*, *43*(3), 1047–1054.

Nakata, N., Chang, J. P., Lawrence, J. F., & Boué, P. (2015). Body wave extraction and tomography at long beach, california, with ambient-noise interferometry. *Journal of Geophysical Research: Solid Earth*, *120*(2), 1159–1173. doi: 10.1002/2015JB011870

Nakata, N., Snieder, R., Tsuji, T., Larner, K., & Matsuoka, T. (2011). Shear wave imaging from traffic noise using seismic interferometry by cross-coherence. *Geophysics*, *76*(6), SA97–SA106.

Obermann, A., Kraft, T., Larose, E., & Wiemer, S. (2015). Potential of ambient seismic noise techniques to monitor the st. gallen geothermal site (switzerland). *Journal of Geophysical Research: Solid Earth*, *120*(6), 4301–4316.

Obermann, A., Lupi, M., Mordret, A., Jakobsdóttir, S. S., & Miller, S. A. (2016). 3d-ambient noise rayleigh wave tomography of snæfellsjökull volcano, iceland. *Journal of Volcanology and Geothermal Research*, *317*, 42–52.

Park, C. B., Miller, R. D., & Xia, J. (1998). Imaging dispersion curves of surface waves on multi-channel record. In *Seg technical program expanded abstracts 1998* (pp. 1377–1380). Society of Exploration Geophysicists.

Paterson, M. S., & Wong, T. (2005). *Experimental rock deformation-the brittle field.* Springer Science & Business Media.

Pazzi, V., Tanteri, L., Bicocchi, G., D'Ambrosio, M., Caselli, A., & Fanti, R. (2017). H/V measurements as an effective tool for the reliable detection of landslide slip surfaces: Case studies of Castagnola (La Spezia, Italy) and Roccalbegna (Grosseto, Italy). *Physics and Chemistry of the Earth*, *98*, 136–153. doi: 10.1016/j.pce.2016.10.014

Perton, M., Spica, Z., & Caudron, C. (2018). Inversion of the horizontal-to-vertical spectral ratio in presence of strong lateral heterogeneity. *Geophysical journal international*, *212*(2), 930–941.

Planès, T., Obermann, A., Antunes, V., & Lupi, M. (2020). Ambient-noise tomography of the greater geneva basin in a geothermal exploration context. *Geophysical Journal International*, *220*(1), 370–383.

Plesinger, A., & Wielandt, E. (1974). Seismic noise at 2 hz in europe. *Journal of Geophysics-zeitschrift Fur Geophysik*, *40*(1), 131–136.

Prieto, G., Lawrence, J., & Beroza, G. (2009). Anelastic earth structure from the coherency of the ambient seismic field. *Journal of Geophysical Research: Solid Earth*, *114*(B7).

Rawlinson, N. (2005). Fmst: fast marching surface tomography package–instructions. *Research School of Earth Sciences, Australian National University, Canberra*.

Rawlinson, N., & Sambridge, M. (2005). The fast marching method: an effective tool for tomographic imaging and tracking multiple phases in complex layered media. *Exploration Geophysics*, *36*(4), 341–350.

Ren, J. (1987). *Geotectonic evolution of china.* Springer Verlag.

Rost, S., & Thomas, C. (2002). Array seismology: Methods and applications. *Reviews of geophysics*, *40*(3), 2–1.

Rubio-Maya, C., Díaz, V. A., Martínez, E. P., & Belman-Flores, J. M. (2015). Cascade utilization of low and medium enthalpy geothermal resources- a review. *Renewable and Sustainable Energy Reviews*, *52*, 689–716.

Santos, P. A., & Rivas, J. A. (2009). Gravity survey contribution to geothermal exploration in el salvador: The cases of berlín, ahuachapán and san vicente areas. *LaGeo SA de CV United Nations University Geothermal Training Program*.

Schimmel, M., & Paulssen, H. (1997). Noise reduction and detection of weak, coherent signals through phase weighted stacks. *Geophysical Journal International*, *130*, 497–505.

Schimmel, M., Stutzmann, E., & Gallart, J. (2011). Using instantaneous phase coherence for signal extraction from ambient noise data at a local to a global scale. *Geophysical Journal International*, *184*(1), 494–506.

Schuster, G., Yu, J., Sheng, J., & Rickett, J. (2003). Interferometric/daylight seismic imaging: Geoph. *J. Int.,(accepted)*.

Shapiro, N. M., & Campillo, M. (2004). Emergence of broadband rayleigh waves from correlations of the ambient seismic noise. *Geophysical Research Letters*, *31*(7).

Snieder, R. (2004). Extracting the green's function from the correlation of coda waves: A derivation based on stationary phase. *Physical Review E*, *69*(4), 046610.

Snieder, R., Miyazawa, M., Slob, E., Vasconcelos, I., & Wapenaar, K. (2009). A comparison of strategies for seismic interferometry. *Surveys in Geophysics*, *30*(4-5), 503–523.

Spica, Z. J., Nakata, N., Liu, X., Campman, X., Tang, Z., & Beroza, G. C. (2018, jul). The Ambient Seismic Field at Groningen Gas Field: An Overview from the Surface to Reservoir Depth. *Seismological Research Letters*, *89*(4), 1450–1466. doi: 10.1785/0220170256

Stehly, L., Campillo, M., & Shapiro, N. (2006). A study of the seismic noise from its long-range correlation properties. *Journal of Geophysical Research: Solid Earth*, *111*(B10).

Strobbia, C., & Cassiani, G. (2011). Refraction microtremors: Data analysis and diagnostics of key hypotheses. *Geophysics*, *76*(3). doi: 10.1190/1.3560246

Sylvette, B.-C., Cécile, C., Pierre-Yves, B., Fabrice, C., Peter, M., Jozef, K., & Fäh, D. (2006). H/v ratio: a tool for site effects evaluation. results from 1-d noise simulations. *Geophysical Journal International*, *167*(2), 827–837.

Thanassoulas, C. (1991). Geothermal exploration using electrical methods. *Geoexploration*, *27*(3-4), 321–350.

Tibuleac, I., & Eneva, M. (2011). Seismic signature of the geothermal field at soda lake, nevada, from ambient noise analysis. *Geothermal Resources Council Transactions*, *35*, 1767–1771.

Tibuleac, I., Von Seggern, D., Louie, J. N., & Anderson, J. (2009). High resolution seismic velocity structure in the reno basin from ambient noise recorded by a variety of seismic instruments. *Geothermal Resources Council Transactions*, *33*, 143–148.

Tomac, I., & Sauter, M. (2018). A review on challenges in the assessment of geomechanical rock performance for deep geothermal reservoir development. *Renewable and Sustainable Energy Reviews*, *82*, 3972–3980.

Van Dalen, K. N., Mikesell, T. D., Ruigrok, E. N., & Wapenaar, K. (2015). Retrieving surface waves from ambient seismic noise using seismic interferometry by multidimensional deconvolution. *Journal of Geophysical Research: Solid Earth*, *120*(2), 944–961.

Vasconcelos, I., & Snieder, R. (2008a). Interferometry by deconvolution: Part 1—theory for acoustic waves and numerical examples. *Geophysics*, *73*(3), S115–S128.

Vasconcelos, I., & Snieder, R. (2008b). Interferometry by deconvolution: Part 2—theory for elastic waves and application to drill-bit seismic imaging. *Geophysics*, *73*(3), S129–S141.

Ventosa, S., Schimmel, M., & Stutzmann, E. (2017). Extracting surface waves, hum and normal modes: time-scale phase-weighted stack and beyond. *Geophysical Journal International*, *211*(1), 30–44.

Wang, G., Zhang, W., Liang, J., Lin, W., Liu, Z., & Wang, W. (2017). Evaluation of geothermal resources potential in china. *Acta Geoscientica Sinica*, *38*(4), 448–459.

Wapenaar, K. (2004a). Retrieving the elastodynamic green's function of an arbitrary inhomogeneous medium by cross correlation. *Physical Review Letters*, *93*(25), 254301.

Wapenaar, K. (2004b). Retrieving the elastodynamic Green's function of an arbitrary inhomogeneous medium by cross correlation. *Physical Review Letters*, *93*(25), 1–4. doi: 10.1103/PhysRevLett.93.254301

Wapenaar, K., Ruigrok, E., van der Neut, J., & Draganov, D. (2011). Improved surface-wave retrieval from ambient seismic noise by multi-dimensional deconvolution. *Geophysical Research Letters*, *38*(1).

Wapenaar, K., van der Neut, J., Ruigrok, E., & van der Neut, J. (2008). Passive seismic interferometry by multidimensional deconvolution. *Geophysics*,

73(NO.6), A51–A56.
Ward, P. L. (1972). Microearthquakes: prospecting tool and possible hazard in the development of geothermal resources. *Geothermics*, *1*(1), 3–12.
Wathelet, M., Jongmans, D., & Ohrnberger, M. (2004). Surface-wave inversion using a direct search algorithm and its application to ambient vibration measurements. *Near surface geophysics*, *2*(4), 211–221.
Weaver, R. L., & Lobkis, O. I. (2001). Ultrasonics without a Source: Thermal Fluctuation Correlations at MHz Frequencies. *Physical Review Letters*, *87*(13), 134301. doi: 10.1103/PhysRevLett.87.134301
Weemstra, C., Draganov, D., Ruigrok, E. N., Hunziker, J., Gomez, M., & Wapenaar, K. (2016). Application of seismic interferometry by multidimensional deconvolution to ambient seismic noise recorded in malargüe, argentina. *Geophysical Journal International*, ggw425.
Woolery, E. W., & Street, R. (2002). 3d near-surface soil response from h/v ambient-noise ratios. *Soil Dynamics and Earthquake Engineering*, *22*(9-12), 865–876.
Wright, P. M., Ward, S. H., Ross, H. P., & West, R. C. (1985). State-of-the-art geophysical exploration for geothermal resources. *Geophysics*, *50*(12), 2666–2696.
Xia, J., Miller, R. D., & Park, C. B. (1999). Estimation of near-surface shear-wave velocity by inversion of rayleigh waves. *Geophysics*, *64*(3), 691–700.
Xie, H., Li, C., Zhou, T., Chen, J., Liao, J., Ma, J., & Li, B. (2020). Conceptualization and evaluation of the exploration and utilization of low/medium-temperature geothermal energy: a case study of the guangdong-hong kong-macao greater bay area. *Geomechanics and Geophysics for Geo-Energy and Geo-Resources*, *6*(1), 18.
Yang, Y., Ritzwoller, M. H., Levshin, A. L., & Shapiro, N. M. (2007). Ambient noise Rayleigh wave tomography across Europe. *Geophysical Journal International*, *168*(1), 259–274.
Yao, H., & van der Hilst, R. D. (2009). Analysis of ambient noise energy distribution and phase velocity bias in ambient noise tomography, with application to SE Tibet. *Geophysical Journal International*, *179*(2), 1113–1132.
Yao, H., van der Hilst, R. D., & de Hoop, M. V. (2006). Surface-wave array tomography in SE Tibet from ambient seismic noise and two-station analysis - I. Phase velocity maps. *Geophysical Journal International*, *166*(2), 732–744. doi: 10.1111/j.1365-246X.2006.03028.x
Yin, X., Xu, H., Mi, B., Hao, X., Wang, P., & Zhang, K. (2020). Joint inversion of rayleigh and love wave dispersion curves for improving the accuracy of near-surface s-wave velocities. *Journal of Applied Geophysics*, *176*, 103939.
Yoon, S., & Rix, G. J. (2009). Near-Field Effects on Array-Based Surface Wave Methods with Active Sources. *Journal of Geotechnical and Geoenvironmental Engineering*, *135*(3), 399–406. doi: 10.1061/(ASCE)1090-0241(2009)135:3(399)
Yuan, Y., Ma, Y., Hu, S., Guo, T., & Fu, X. (2006). Present-day geothermal characteristics in south china. *Chinese Journal of Geophysics*, *49*(4), 1005–1014.
Zaher, M. A., Saibi, H., Mansour, K., Khalil, A., & Soliman, M. (2018). Geothermal exploration using airborne gravity and magnetic data at siwa oasis, western desert, egypt. *Renewable and Sustainable Energy Reviews*, *82*, 3824–3832.
Zhang, L., Chen, S., & Zhang, C. (2019). Geothermal power generation in china: Status and prospects. *Energy Science & Engineering*, *7*(5), 1428–1450.
Zhejiang, B. (1989). Regional geology of zhejiang province. In *Geological memoirs 1 (11), the ministry of geology and mineral resources.* Geological Publishing House Beijing.
Zhu, T., & Stensrud, D. J. (2019). Characterizing Thunder-Induced Ground Motions Using Fiber-Optic Distributed Acoustic Sensing Array. *Journal of Geophysical Research: Atmospheres*, 810–823. doi: 10.1029/2019JD031453

Table 1. Prior boundaries of uniform probability distributions used for each parameter of the depth model.

Layer number	**Thickness**(km)	**Poisson ratio**	$\mathbf{V_s}(km/s)$	$\boldsymbol{Density}(g/cm^3)$
01	$0.01 \sim 0.03$	$0.2 \sim 0.5$	$1.3 \sim 2.3$	$1.9 \sim 2.6$
02	$0.02 \sim 0.04$	$0.2 \sim 0.5$	$1.5 \sim 2.8$	$2.0 \sim 2.7$
03	$0.02 \sim 0.06$	$0.2 \sim 0.5$	$1.7 \sim 3.2$	$2.0 \sim 2.8$
04	$0.03 \sim 0.08$	$0.2 \sim 0.5$	$1.8 \sim 3.4$	$2.0 \sim 2.8$
05	$0.04 \sim 0.10$	$0.2 \sim 0.5$	$1.9 \sim 3.5$	$2.1 \sim 2.8$
06	$0.05 \sim 0.13$	$0.2 \sim 0.5$	$2.0 \sim 3.6$	$2.1 \sim 2.8$
07	$0.07 \sim 0.18$	$0.2 \sim 0.5$	$2.0 \sim 3.7$	$2.1 \sim 2.9$
08	$0.09 \sim 0.23$	$0.2 \sim 0.5$	$2.0 \sim 3.8$	$2.1 \sim 2.9$
09	$0.12 \sim 0.31$	$0.2 \sim 0.5$	$2.1 \sim 3.9$	$2.1 \sim 2.9$
10	$0.16 \sim 0.41$	$0.2 \sim 0.5$	$2.2 \sim 4.0$	$2.1 \sim 2.9$
11	$0.21 \sim 0.55$	$0.2 \sim 0.5$	$2.3 \sim 4.2$	$2.2 \sim 3.0$
12	$0.28 \sim 0.73$	$0.2 \sim 0.5$	$2.4 \sim 4.4$	$2.2 \sim 3.0$
half-space	$0.28 \sim 0.73$	$0.2 \sim 0.5$	$2.4 \sim 4.5$	$2.2 \sim 3.0$

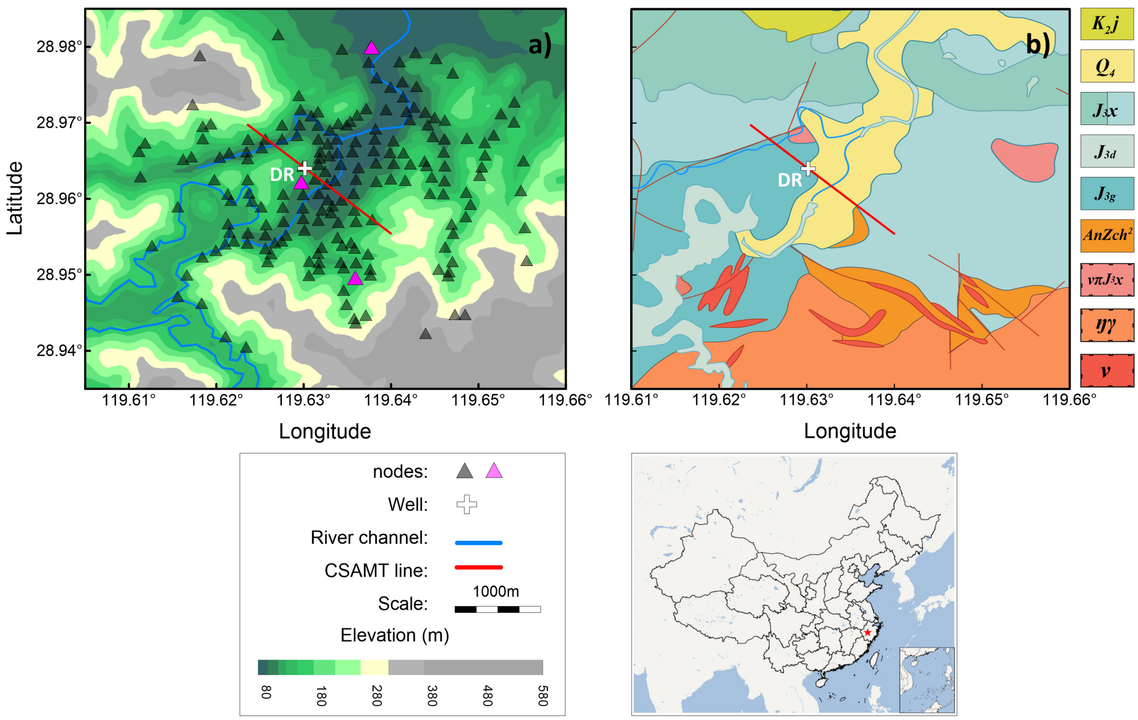

Figure 1. Maps of the geothermal site and the Andi network. (a). Topography map of the survey region and available seismic nodal network. The triangles denote the Zland nodes; three magenta triangles denote three stations used in spectral analysis; the white cross denotes the well location; the red line indicates the CSAMT profile line; the blue curves indicate the river channel as well as the water reservoir outlines located in the southwest. (b). Geology map of the survey region. K_2j denotes the Cretaceous system; Q_4 denotes the Quaternary system; J_3x, J_3d, and J_3g denote three different groups of the upper Jurassic system; $AnZch^2$ denotes the PreSinian system; $\nu\pi J_3x$ indicates the felsophyre; $\eta\gamma$ denotes the coarse-grained adamellites; ν denotes the granite dykes. The red star on China map indicates the location of the Andi town.

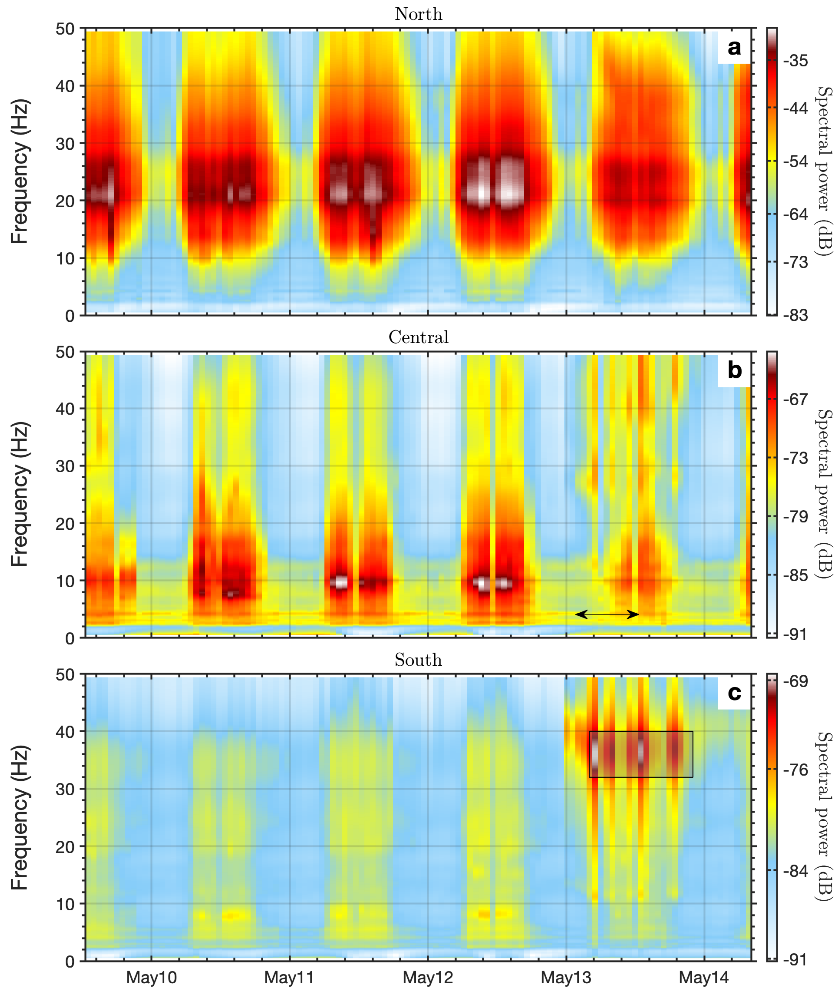

Figure 2. Vertical component spectrograms of over 4 days ambient noise data at three different stations, north (a), central (b) and south (c). The three stations are denoted by the three magenta triangles on Fig.1a. The black double-arrow on b indicates the spectrum of consistent sources from anthropogenic activities. The gray box on c highlights the source spectrum from the rain- and thunder-induced ground motions.

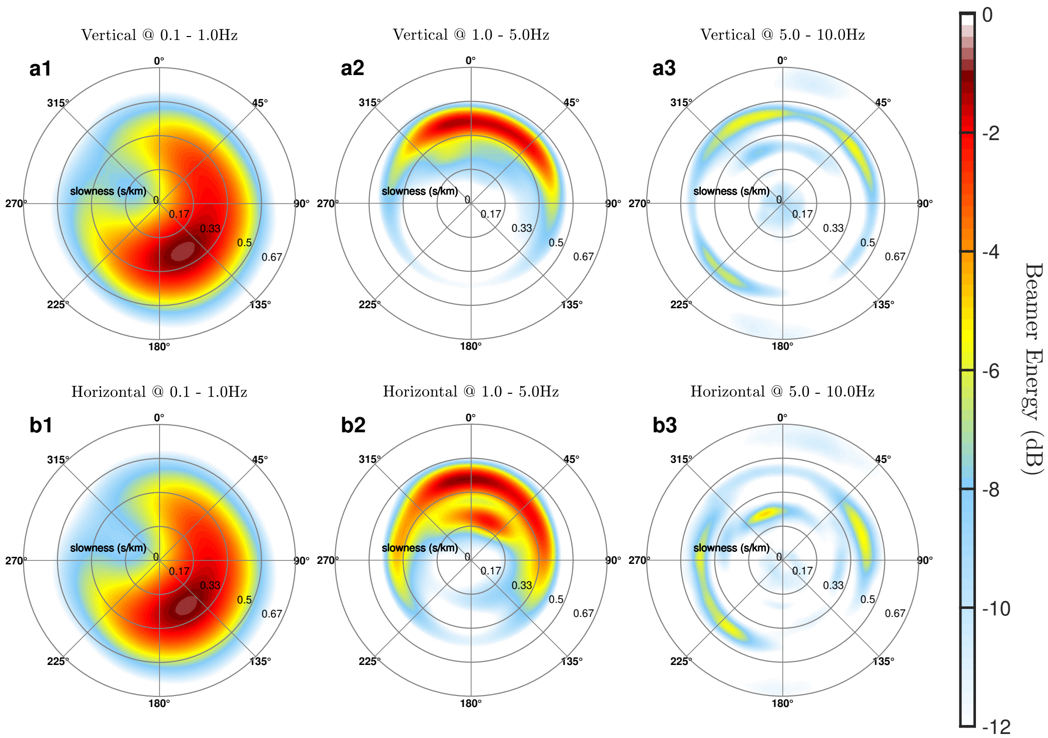

Figure 3. Beamforming analysis performed on the vertical component (the upper panels, a1, a2, a3) and the north horizontal component (the bottom panels, b1, b2, b3) of Andi network at different frequency bands 0.1-1.0Hz (a1, b1), 1.0-5.0Hz (a2, b2) and 5.0-10Hz (a3,b3).

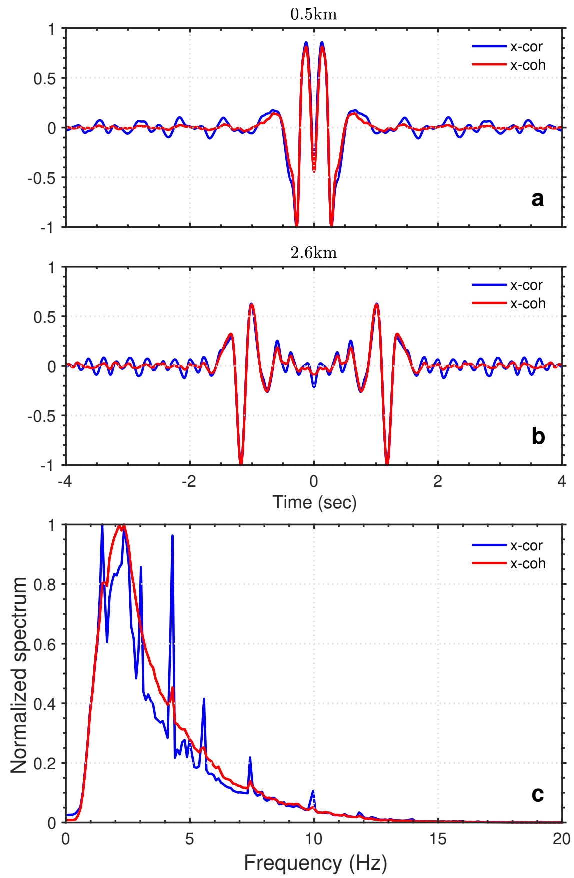

Figure 4. Comparisons between the bin-stacked cross-correlation (the blue curves) and cross-coherence (the red curves) functions with interstation distance at 0.5km (a) and 2.6km (b). (c) Comparison between the averaged spectrum from the bin-stacked virtual-source gathers from cross-correlation and cross-coherence (see Fig.S1 in the supporting information).

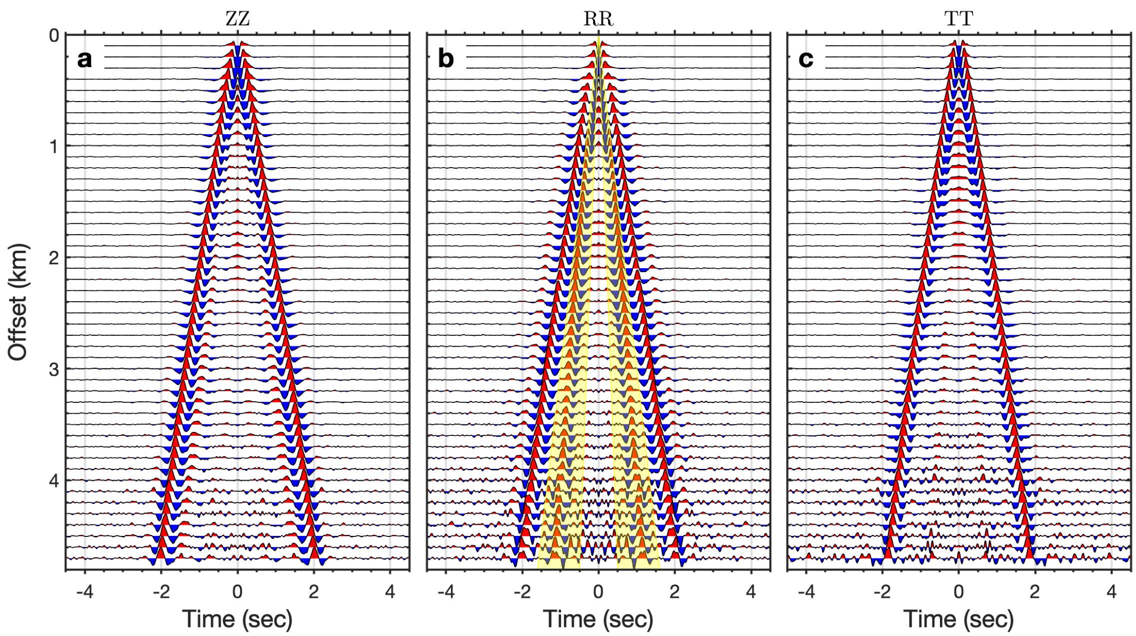

Figure 5. Bin-stacked virtual-source gathers from Z-Z (a), R-R (b), and T-T (c) cross-coherence functions. Bandpass filter between 1 and 10Hz has been applied. The body waves are highlighted by yellow color on b.

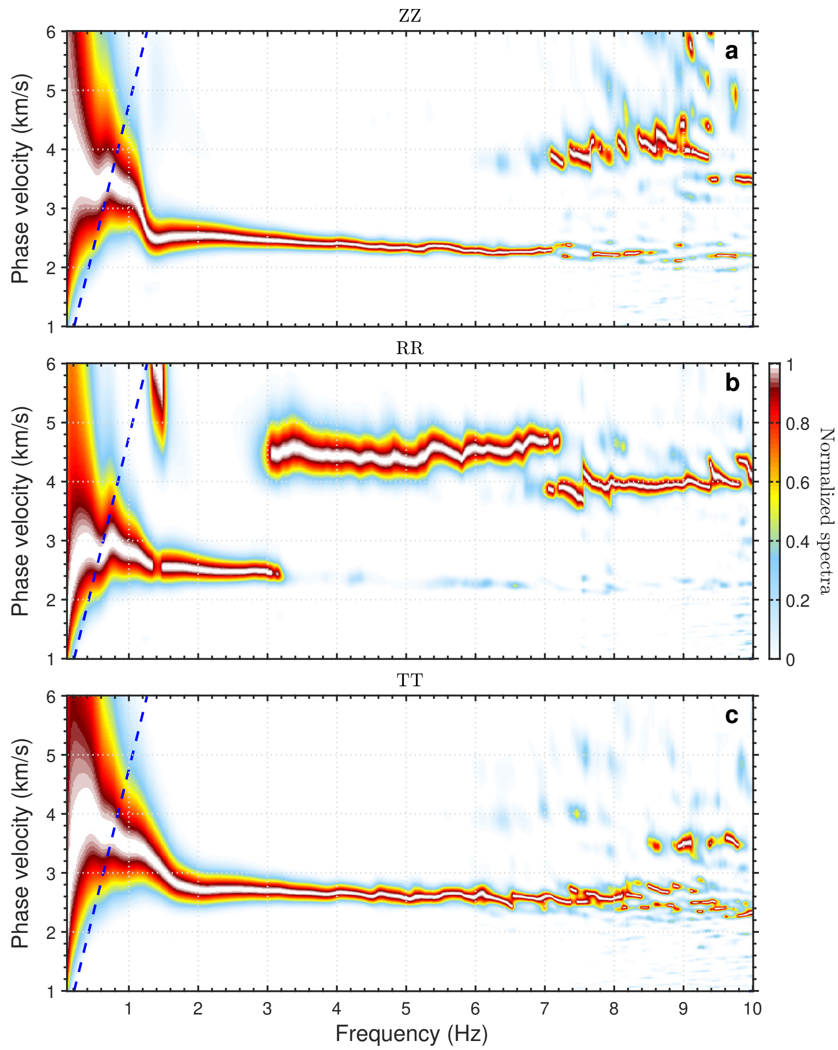

Figure 6. Dispersion measurements from the bin-stacked virtual-source gathers at Z-Z component (a), and R-R component (b), and T-T component (c). The blue dash lines indicate the minimum wavenumber defined by $k_{min} = \frac{1}{Array\ length}$.

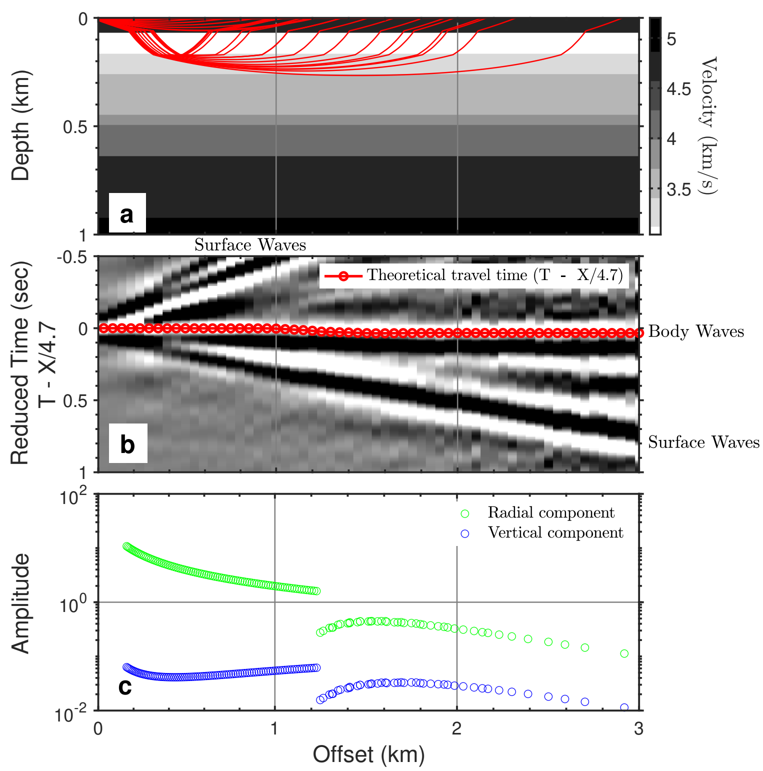

Figure 7. (a) 1D velocity model used for ray tracing as derived from smoothed sonic log and resulting ray geometry of the P-wave. (b) Superposition of the theoretical raytracing travel times on the interferometric wave field of the bin-stacked R-R component. Traveltimes are corrected with a linear move-out velocity of 4.7km/s. Bandpass filter between 4 and 10Hz has been applied. (c) Ray tracing amplitudes of the radial and vertical components.

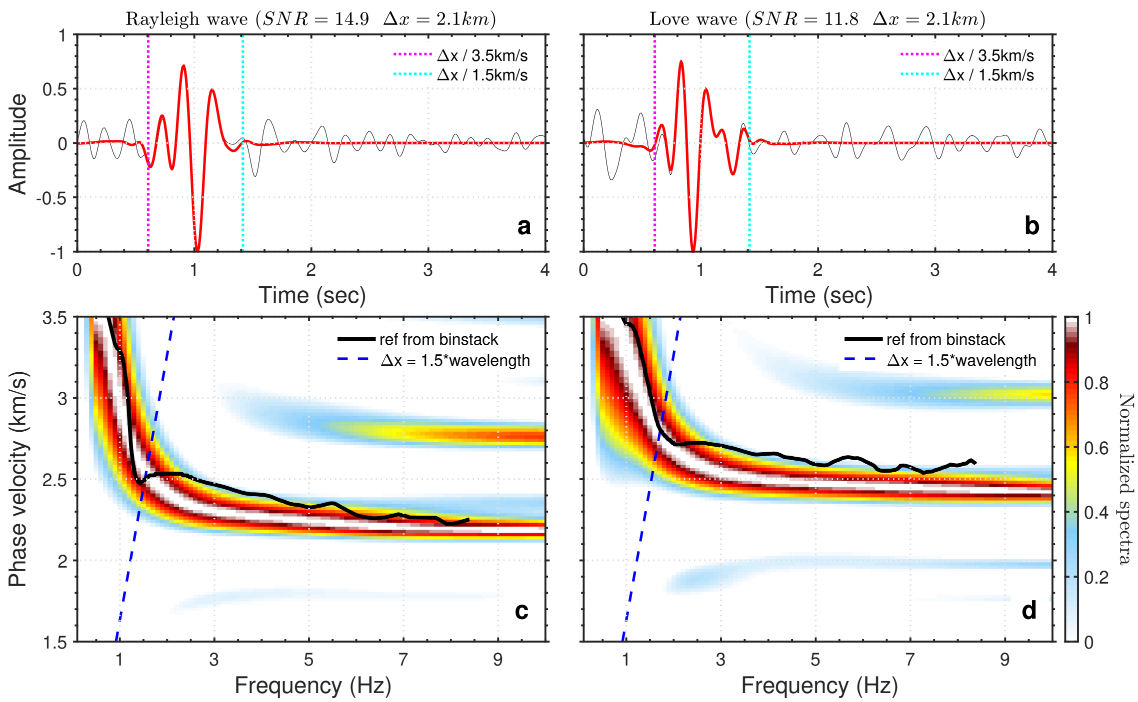

Figure 8. Examples of dispersion analysis for Rayleigh wave (left panels) and Love wave (right panels) using the image transformation technique by Yao et al. (2006). The thin black and red curves on a and b present the empirical Green's functions before and after velocity filter (or mute) with velocity range from 1.5km/s to 3.5km/s. Colored dashed lines indicate the time window estimated from the corresponding velocity window. For better presentation, all EGFs have been bandpass filtered (1∼10Hz). The thick black curves on c and d present the reference average dispersion curves picked from Fig.6. The blue dashed lines indicate the 1.5 times wavelength criterion.

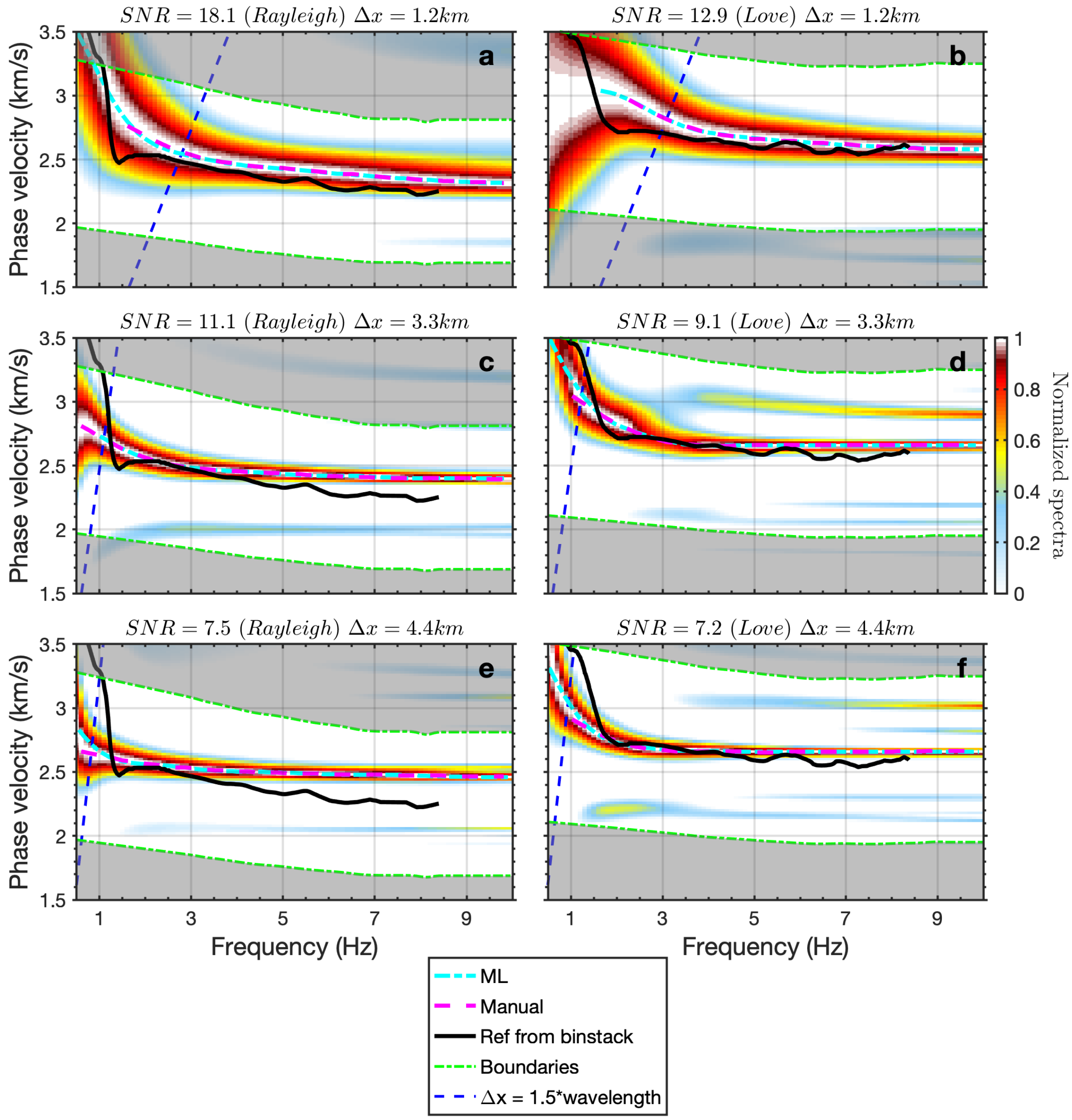

Figure 9. Examples of dispersion curves picking for Rayleigh waves (left panels) and Love waves (right panels) using Machine Learning. The cyan curves indicate the picked dispersion curves using ML technique; the magenta curves indicate the manually picked dispersion curves; the black curves indicate the reference average dispersion curves picked from Fig.6; the green curves indicate the upper and bottom boundaries defined by the smoothed reference dispersion curves; the blue lines indicate the 1.5 times wavelength criterion. We mask the dispersion spectra beyond the confidence region. We label each sub-figure with the corresponding SNR, wave type and the interstation distance.

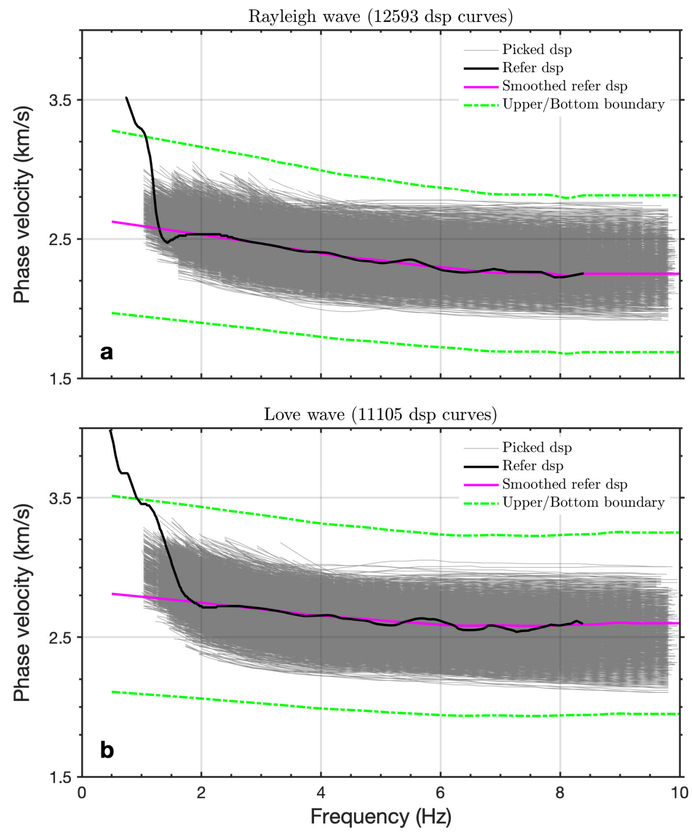

Figure 10. Picked dispersion curves for Rayleigh waves (a) and Love waves (b) by using Machine Learning. The think gray curves indicate the final picked dispersion curves using ML technique; the black curves indicate the reference average dispersion curves picked from Fig.6; the magenta curves indicate the smoothed reference dispersion curves; the green curves indicate the upper and bottom boundaries defined by the smoothed reference dispersion curves. We label each sub-figure with the corresponding wave type and the total number of the picked dispersion curves.

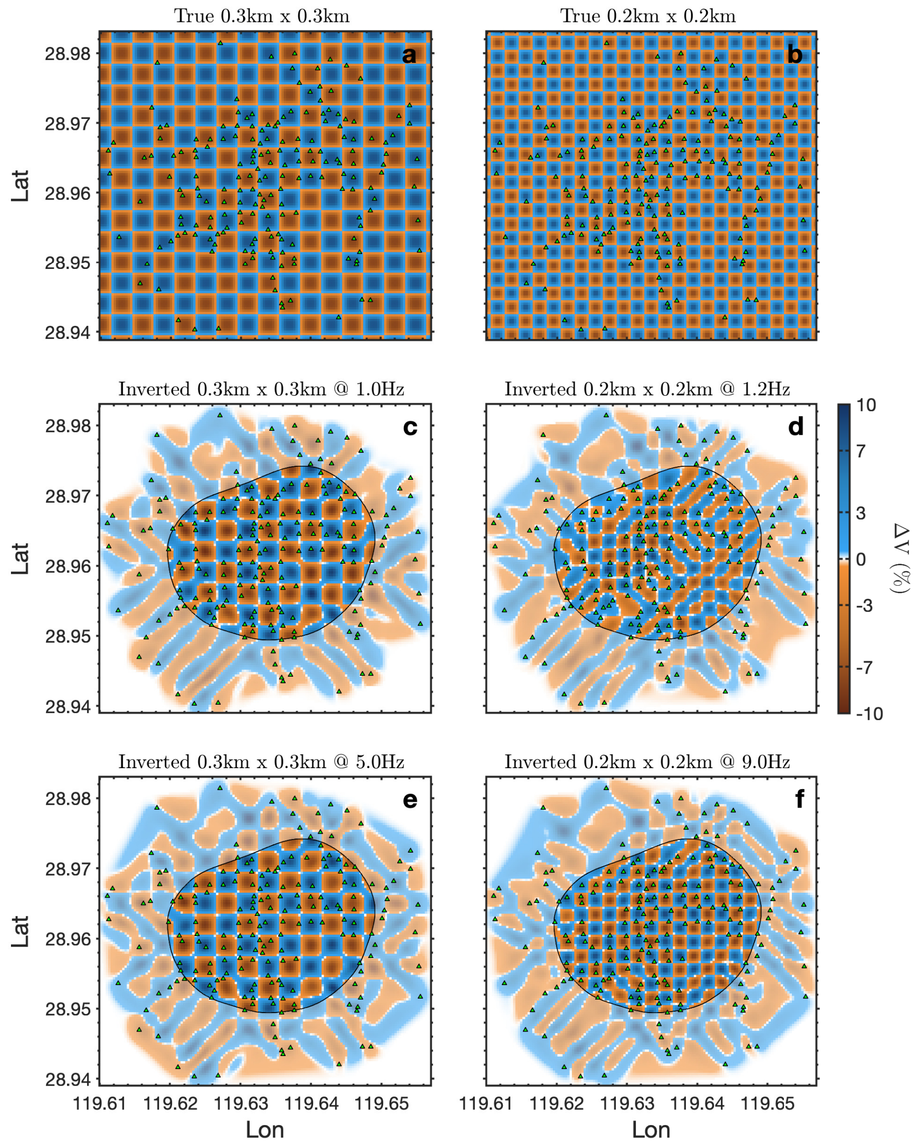

Figure 11. Checkerboard tests for surface wave tomography with two spatial resolutions, 0.3km (the left panels) and 0.2km (the right panels). (a) and (b) present the simulated models; (c-f) present the recovered models at different frequencies, 1.0Hz, 1.2Hz, 5.0Hz, and 9.0Hz. The green triangles denote the seismic network; the black contours indicate the resolvable zone defined with raypath density. We mask the area beyond the resolvable zone. Here we consider the Love waves as an example.

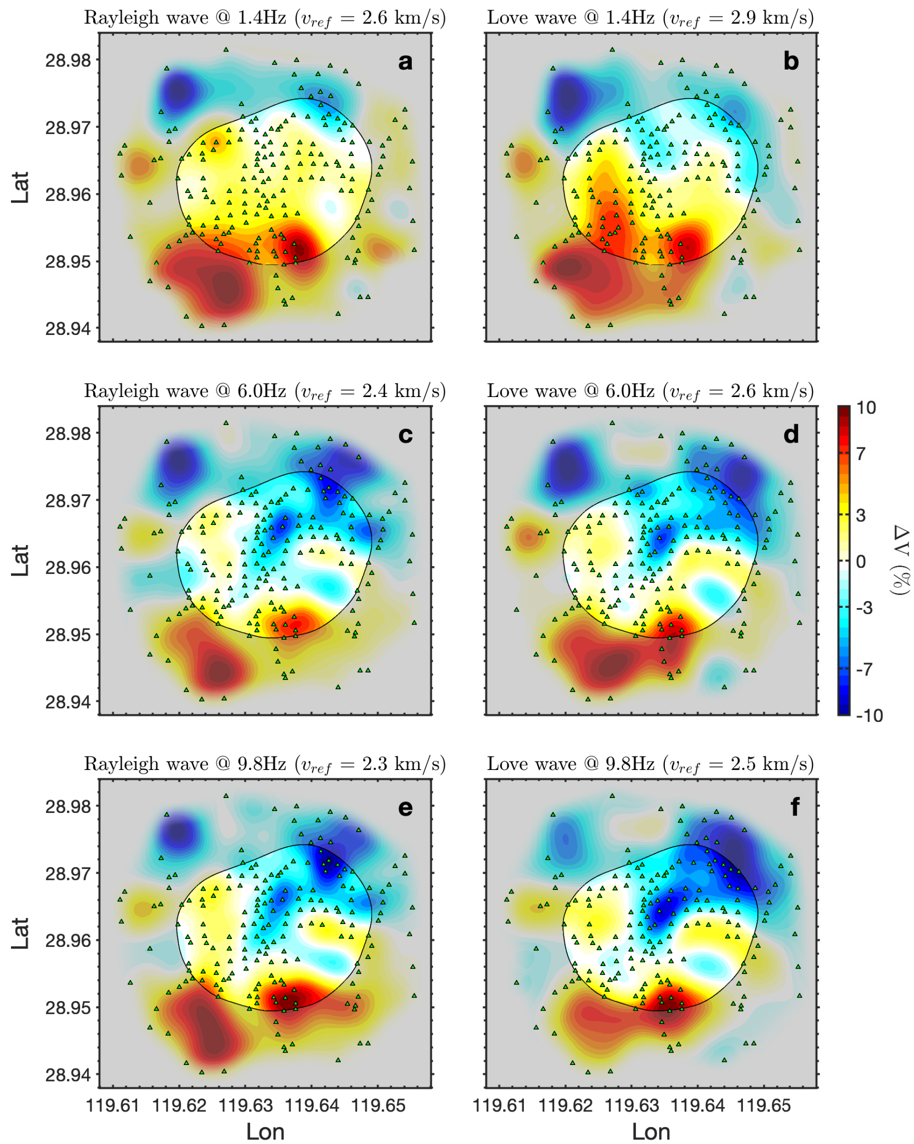

Figure 12. Phase velocity tomographic results for Rayleigh waves (the left panels) and Love waves (the right panels) at different frequencies, 1.4Hz (a and b), 6.0Hz (c and d), 9.8Hz (e and f). The green triangles denote the seismic network; the black contours indicate the resolvable zone defined with raypath density. We mask the area beyond the resolvable zone.

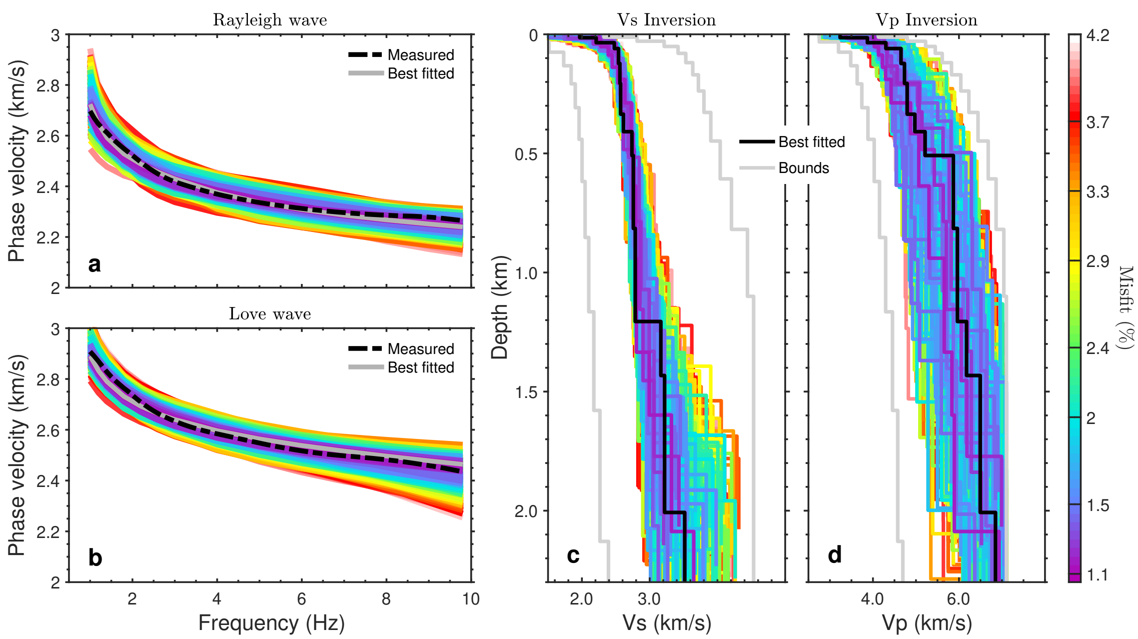

Figure 13. Joint inversion of Rayleigh wave and Love wave dispersion curves. (a) and (b) present examples of the measured (the black dashed curves) and the best 500 forwarded (the colored curves) dispersion curves; the gray curves indicate the best fitted dispersion curves. (c) and (d) present the best 500 Vs and Vp models; the black curves indicates the best fitted model; the gray curves indicate the upper and bottom velocity boundaries. Colors are coded by misfits as shown on the color map.

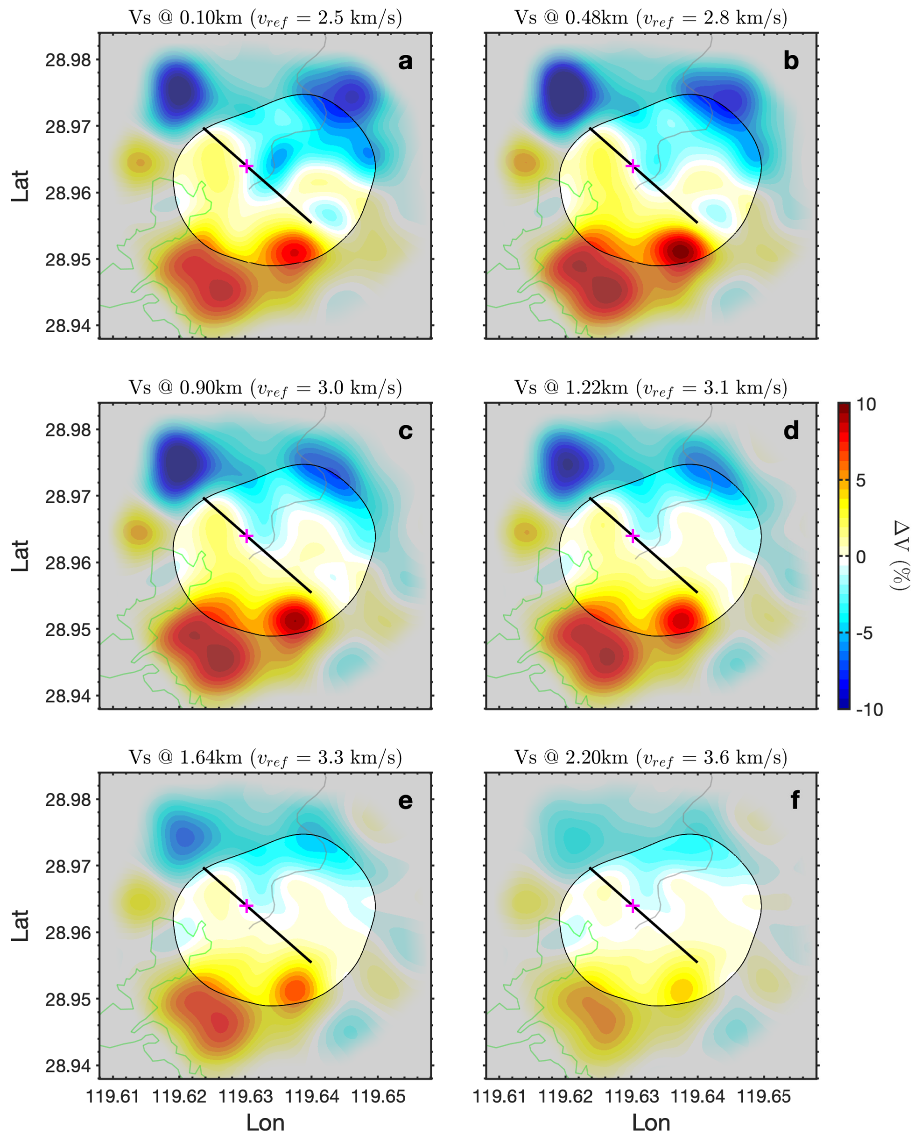

Figure 14. Horizontal slices of the obtained S wave velocity model at different depths. The thick black line indicates the CSAMT profile line; the magenta cross indicates the well location; the think contour indicates the resolvable zone. We mask the area beyond the resolvable zone. We label each sub-figure with the corresponding depth and the reference velocity.

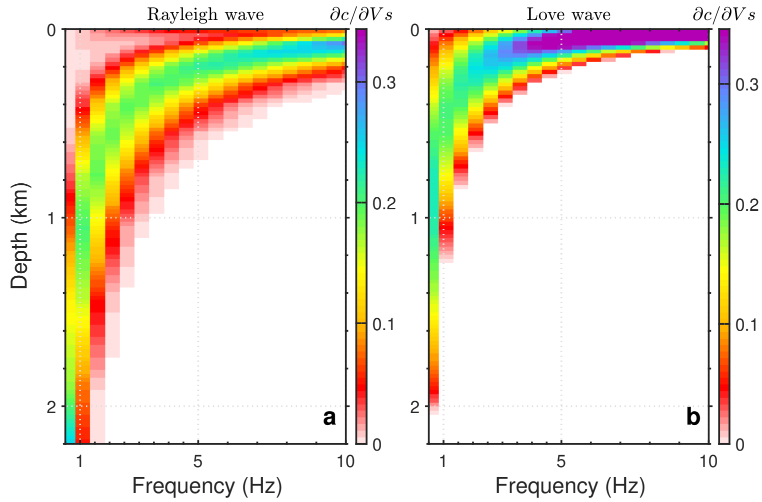

Figure 15. Sensitivity kernels of Rayleigh (a) and Love wave (b) based on the 1D velocity model at the well location.

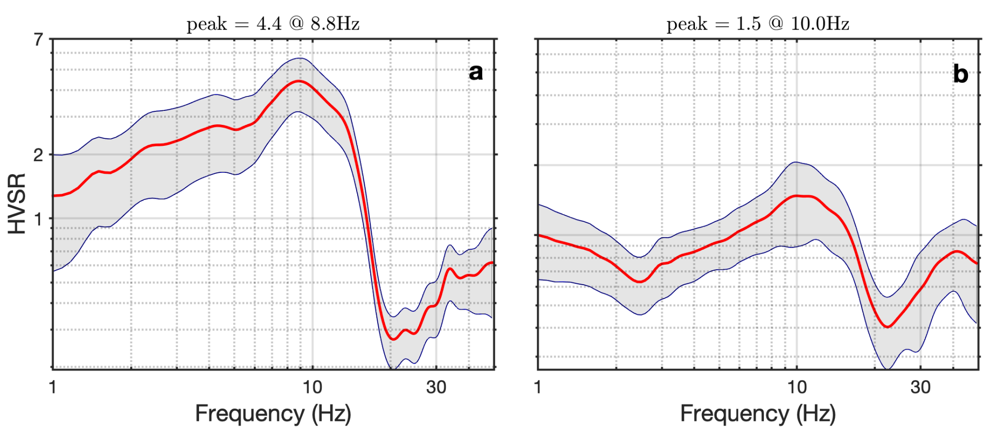

Figure 16. Examples of the obtained HVSR curves at north (a) and south (b). The red curves denote the measured HVSR curves; the blue curves indicate the measurement precisions defined by 0.6 times of the standard deviation.

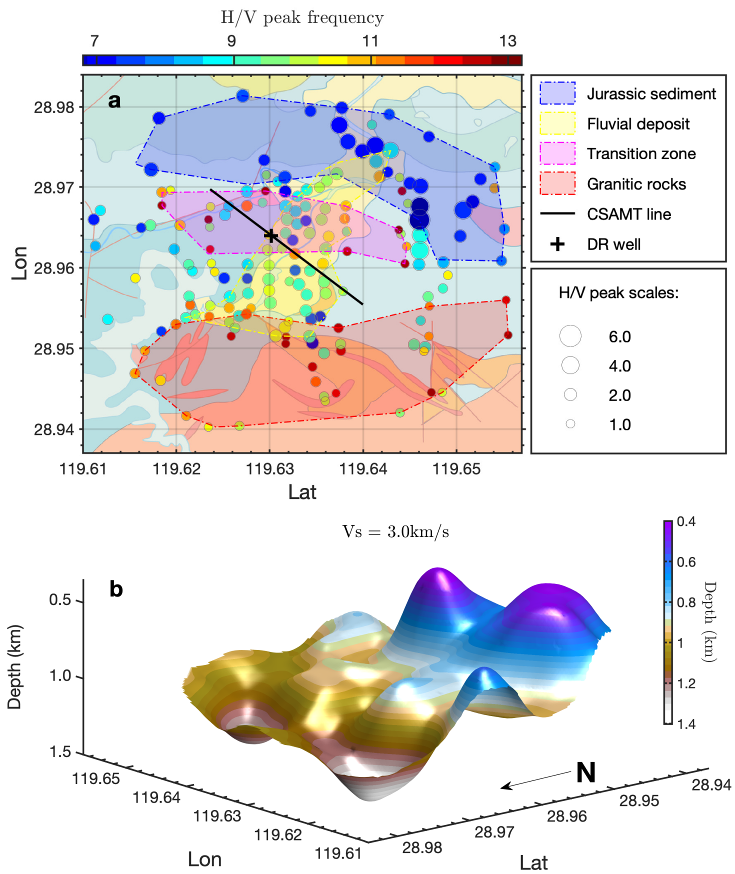

Figure 17. (a). The distribution map of the measured HVSR peaks overlaying on the surface geology map. The scatters denote the HVSR peaks from different stations. The scatter colors are coded by the HVSR peak frequencies; the scatter sizes are scaled by the HVSR peak values. The black line indicates the CSAMT profile line; the cross indicates the well location. Four colored shadows present four main clusters of HVSR measurements as indicated on the legend box. (b). The iso-surface of the median velocity of the inverted Vs model with $V_s = 3.0km/s$. The surface colors are coded by depths.

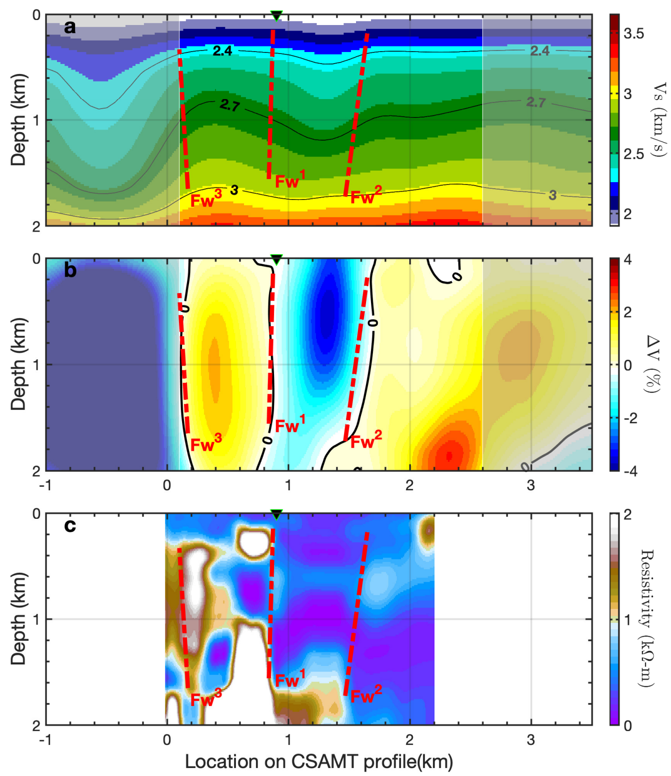

Figure 18. Vertical sections of the obtained S wave velocity model, (a) the absolute velocity model and (b) the velocity variation model, along the CSAMT profile (c). The red dashed lines indicate the inferred fault. We mask the sections beyond the resolvable zone on a and b.

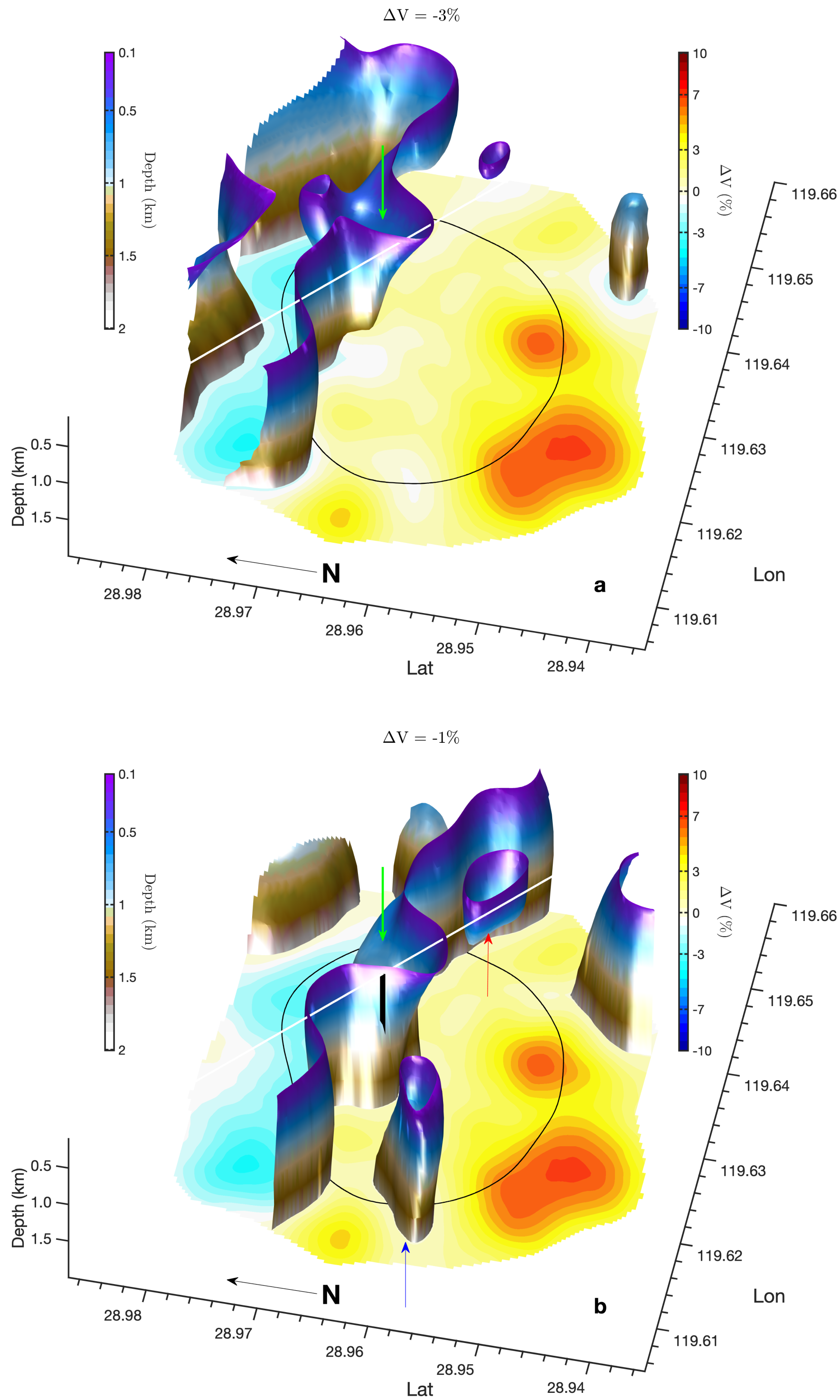

Figure 19. 3-D iso-surface of the obtained Vs variations at $\Delta V = -3\%$ (a) and $\Delta V = -1\%$ (b). The horizontal slice on a and b present the plane Vs variation at depth 2.0km. The black contour on a and b indicate the resolvable zone; the white line on a and b indicate the CSAMT profile line; the green arrow on a an b indicate the interpreted geothermal reservoir channel; the black arrow on b indicates the possible artifacts caused by water reservoir; the red arrow on b indicates the shallow low-velocity anomalies. Colors of the iso-surfaces are coded by depths; colors on the horizontal slices are coded by the velocity variations.

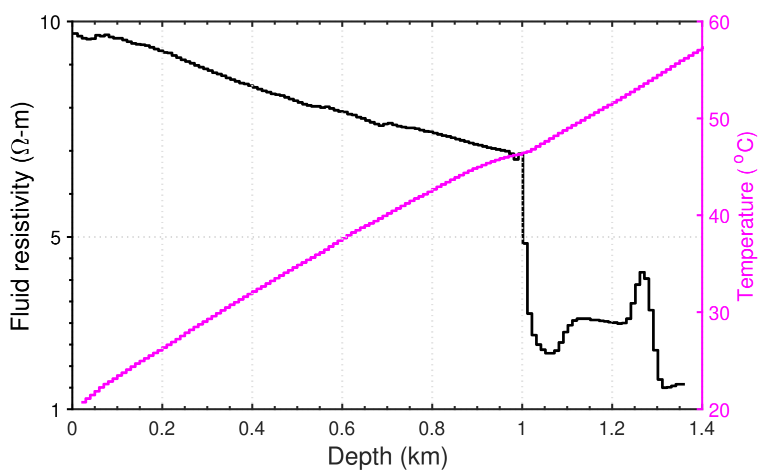

Figure 20. Well log of fluid resistivity (the black curve) and temperature (the magenta curve).

Supporting Information for "Cheng et al., High-resolution ambient noise imaging of geothermal reservoir using dense seismic nodal array and ultra-short observation"

Contents of Supporting Information

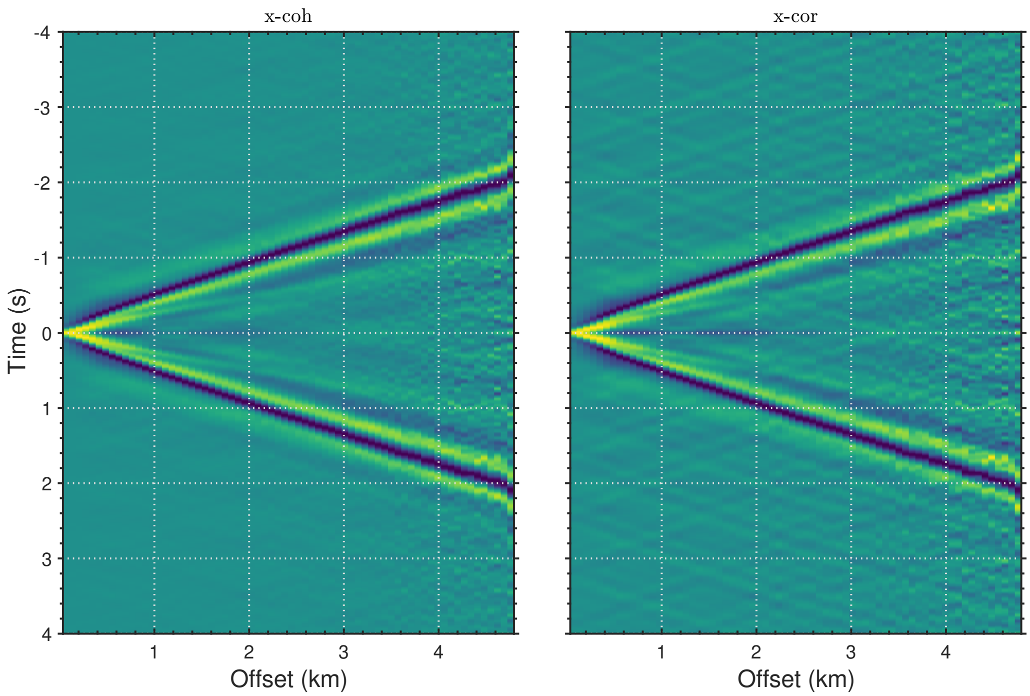

Figure S1. Comparison of the bin-stacked virtual-source gathers between cross-coherence (left) and cross-correlation (right) at vertical component.

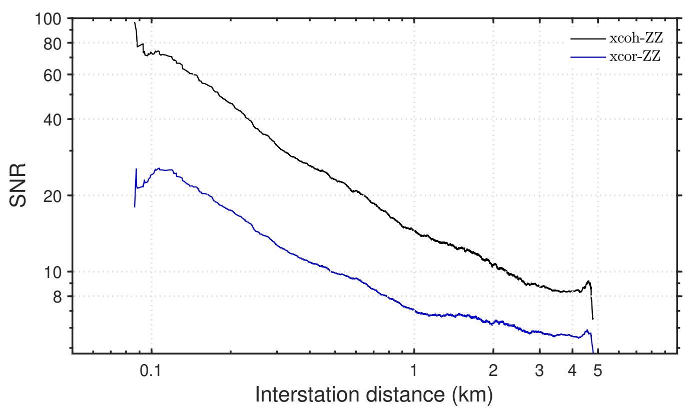

Figure S2. Comparison of SNR between extracted cross-coherence functions (black) and cross-correlation functions (blue). SNR curves have been smoothed for better display.

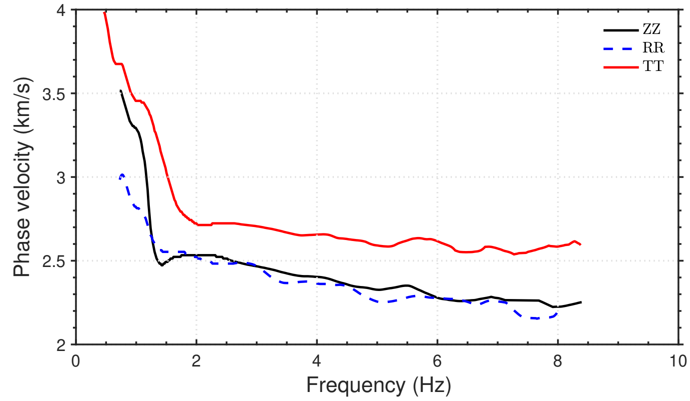

Figure S3. The reference dispersion curves picked from Fig.6 for Z-Z component (black), R-R component (blue) and T-T component (red).

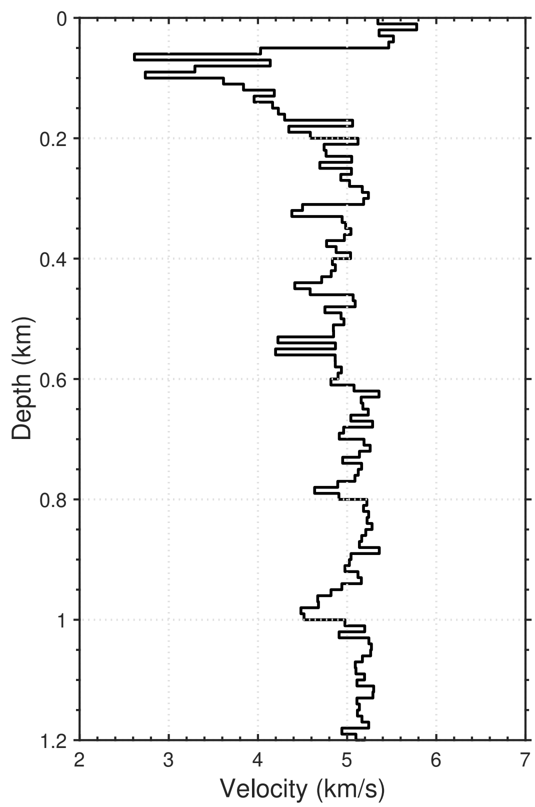

Figure S4. Sonic log from the center of the area (white cross on Fig.1).

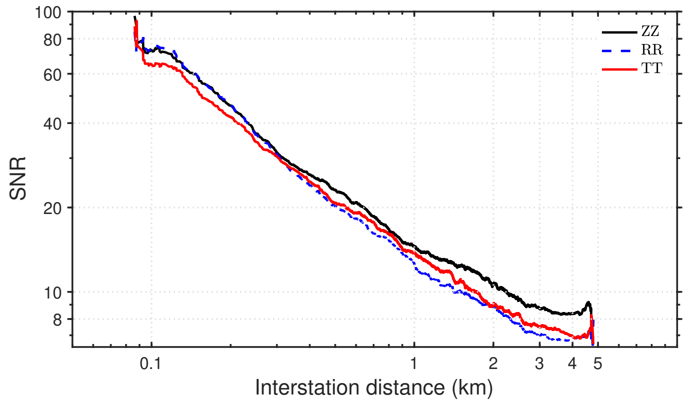

Figure S5. Comparison of SNR of cross-coherence functions between Z-Z component (black), R-R component (blue) and T-T component (red). SNR curves have been smoothed for better display.

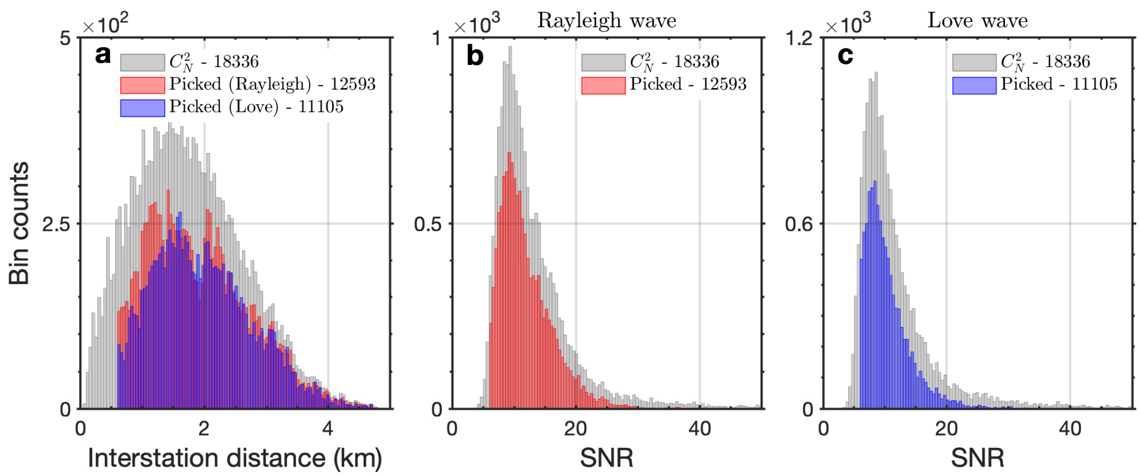

Figure S6. Histograms of interstation distances and SNRs of the picked dispersion curves. (a) Histograms of the interstation distances of all C_N^2 interstation pairs (gray), all picked Rayleigh waves (red), and all picked Love waves (blue). (b) Histograms of SNRs of all C_N^2 interstation pairs (gray) and all picked Rayleigh waves (red). (c) Histograms of SNRs of all C_N^2 interstation pairs (gray) and all picked Love waves (blue).

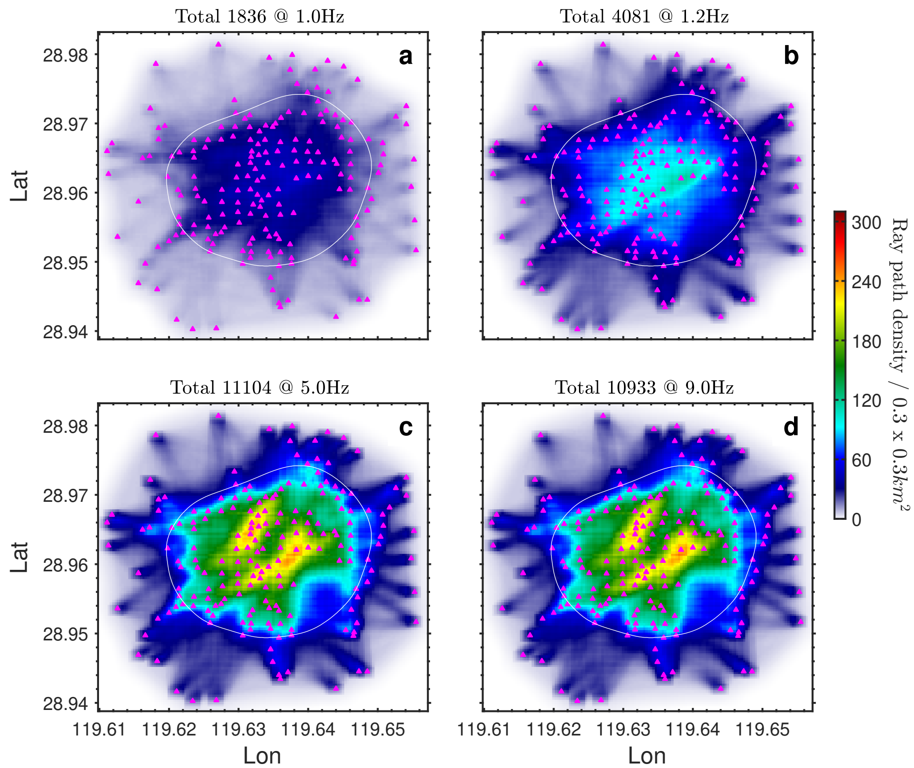

Figure S7. Raypath density maps of Love wave at different frequencies. The magenta triangles denote the seismic network. The white contour indicates the resolvable zone defined by raypath density map of Love wave at 5.0Hz. We label each sub-figure with the corresponding raypath number and frequency.

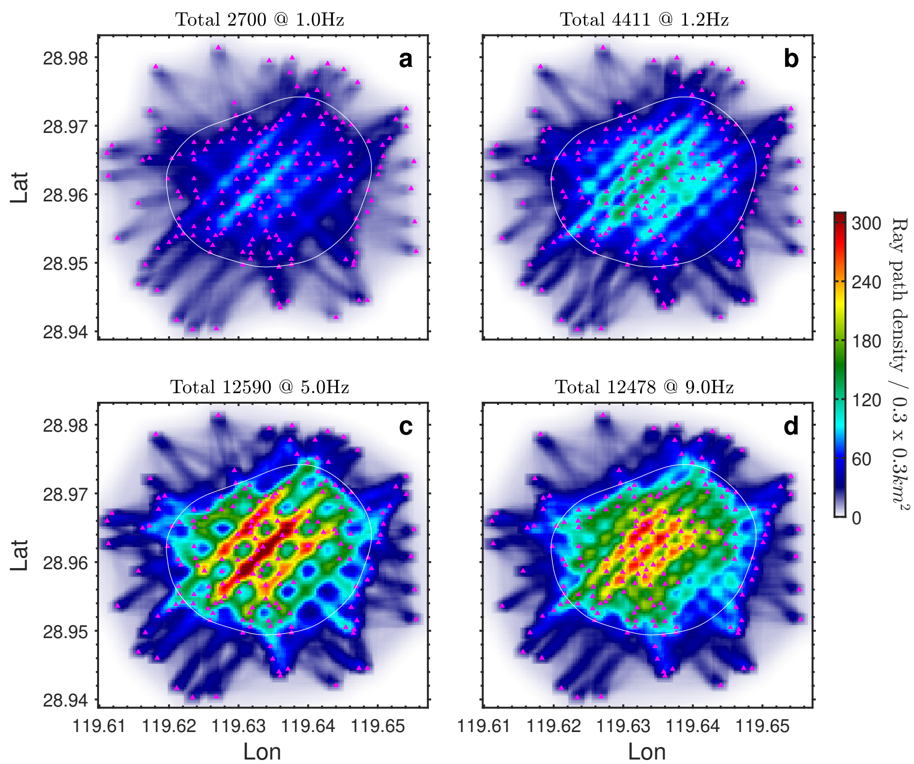

Figure S8. Raypath density maps of Rayleigh wave at different frequencies. The magenta triangles denote the seismic network. The white contour indicates the resolvable zone defined by raypath density map of Love wave at 5.0Hz. We label each sub-figure with the corresponding raypath number and frequency.

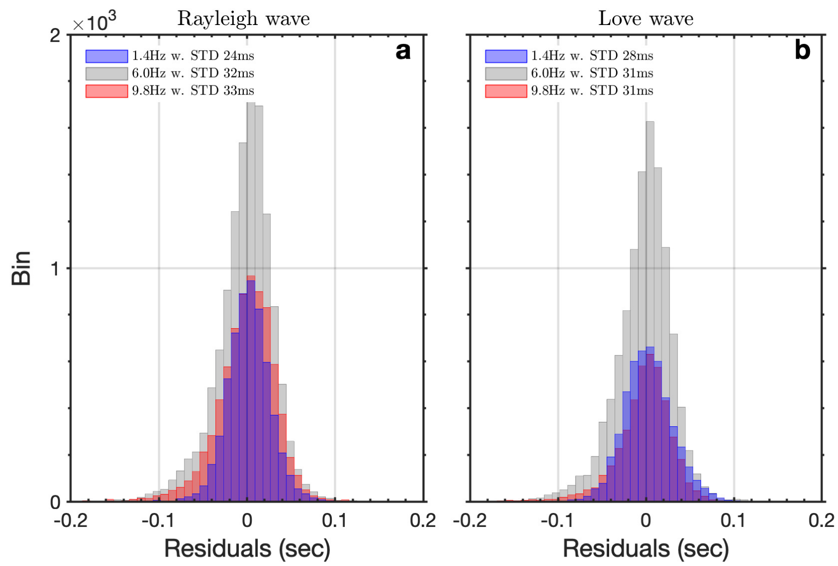

Figure S9. Histograms of the final residuals of surface wave traveltime tomography. (a) and (b) present the residuals for Rayleigh wave tomography and Love wave tomography. The different colors, blue, gray and red, indicate three different frequencies presented on Fig.12. The standard deviations are indicated on the legends.

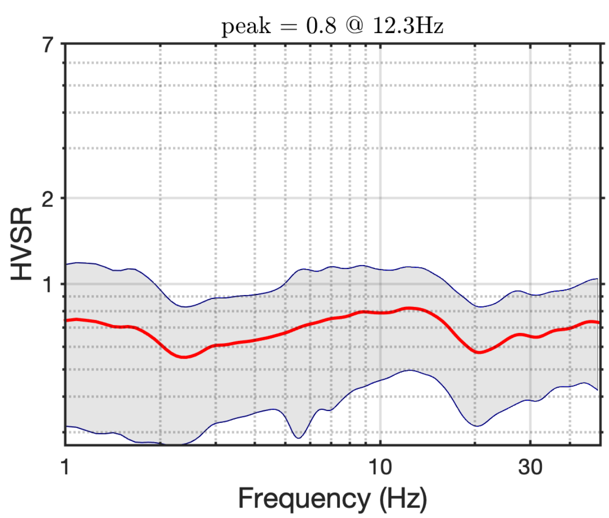

Figure S10. Example of the rejected HVSR curve.